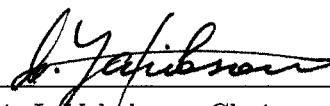RICE UNIVERSITY

Atomistic Modeling of Nano-Materials: From Classical to *ab initio* Simulations in Different Timescales
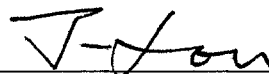
by

Yu Lin

A Thesis Submitted
in Partial Fulfillment of the
Requirements for the Degree

DOCTOR OF PHILOSOPHY

APPROVED, Thesis Committee:

Boris I. Yakobson, Chair
Professor of Mechanical Engineering &
Materials Science, and Chemistry

Jun Lou
Professor of Mechanical Engineering &
Materials Science

Anatoly B. Kolomeisky
Professor of Chemistry

Houston, Texas

November, 2007

UMI Number: 3309907

INFORMATION TO USERS

The quality of this reproduction is dependent upon the quality of the copy submitted. Broken or indistinct print, colored or poor quality illustrations and photographs, print bleed-through, substandard margins, and improper alignment can adversely affect reproduction.

In the unlikely event that the author did not send a complete manuscript and there are missing pages, these will be noted. Also, if unauthorized copyright material had to be removed, a note will indicate the deletion.

UMI®

ABSTRACT

Atomistic Modeling of Nano-Materials: From Classical to *ab initio* Simulations in Different Timescales

by

Yu Lin

Quickly developing computer techniques empower numerical simulations in materials science, which connect abstract theories and empirical experiments. Both deterministic molecular dynamics simulation and stochastic Monte Carlo simulation can employ various levels of theoretical models, from classical potential to the state-of-the-art *ab initio* method, for different simulation accuracies and needs. After the overview of a variety of methods used in this thesis, namely, classical potential, tight-binding (TB), semi-empirical, and density functional theory (DFT) methods, three following examples demonstrate how the computer-assisted simulations enable us to investigate and predict physical and chemical properties of the nano-materials. Mass diffusion through the graphene layer is the first example, where the DFT saddle point calculations are performed to identify the transition states of carbon absorption, ad-dimer flipping over the graphene layer, and C_2 molecule dissociation. In the second

example on the cross-linked carbon nanotube bundles, tight-binding method is used for cross-link modeling and energetic stability analysis. Based on the semi-empirical molecular dynamics simulations of the tensile strength testing, a phenomenological model is proposed. After all the parameters are extracted from the quantum chemistry calculations, a series of canonical Monte-Carlo simulations are conducted to statistically analyze the mechanical properties of a nanotube bundle with thousands of cross-links. The last example on silicon nanowire demonstrates how various methods in different levels can be bridged by the energy decomposition in the energetic analysis. A novel electro-mechanical property of the pentagonal silicon nanowire is predicted by the electronic band structure calculations.

Acknowledgments

The author is greatly thankful to his mentor Boris I. Yakobson for his invaluable guidance, generous support, continuous encouragement, and inspiring enthusiasm devoted to science, which have a great impact on not only his academic study and research, but also on his entire future professional career. He deserves the author's first, and the most earnest acknowledgment. Sincere thanks are expressed to the professors Jun Lou and Anatoly B. Kolomeisky for serving as members of the author's thesis committee and their influence as intructors during his academic years.

Thanks are also due to all his current and former colleagues in the author's department, especially, Feng Ding, Yufeng Zhao, Nevill Gonzalez Szwacki, Amir A. Farajian, Olga V. Pupysheva, Xiuhua Si, Ming Hua, Mingqi Wu, Kun Jiao, Arta Sadrzadeh, and Pavel O. Krasnov. Their daily favor to the author has never ceased for more than five years. Without them, the author can never achieved all that is written in this dissertation.

The final, but the most heartfelt, acknowledgment must go to the author's wife Dongyu. Without her unconditional love, support, encouragement, and companionship, this thesis has no way to be finished; this dissertation is dedicated to her.

Contents

List of Figures

List of Tables

Chapter 1

Simulation Methods and Models

Theory and experiment are two fundamental methodologies to quantitatively investigate the physical world in all scientific disciplines. Due to the current powerful and quickly developing computer technology, numerical simulation is becoming more and more important in both academia and industry. Simulation is an extension of the abstract theories, which are based on both experimental evidence and proposed hypothesis. Nevertheless, the purpose of simulation is to bridge the theoretical hypothesis and the experimental observables, which cannot be achieved or are impractical to obtain. Computational simulation is able to provide a much more transparent understanding of the physical world, which concise theories cannot explain, and current experimental technologies cannot reach, such as the nano-structures.

In this chapter, we start with the molecular description of a material, which is different from the classical continuum description. A variety of theories are introduced to describe how atoms in the materials interact with each other, namely, classical force field model, tight-binding (TB) model, semi-empirical model, and first principle (or *ab initio*) model. Based on these theoretical models, all the static physical properties

for any given material can be computed in principle, including Young's modulus, electronic conductivity, optical absorption, *etc.* For the thermodynamic properties, two basic simulation techniques in nano-materials science, molecular dynamics simulation and Monte Carlo simulation are primarily used.

With different combinations of these methods and models, we investigate various systems from carbon nanostructures to silicon nanowire, and demonstrate the advantages and limitations of each method in the latter chapters.

1.1 Theoretical Models

All computer simulations are based on one or several theories, by which the computer program can describe and simulate the materials. Finite element (FE) is one of the most successful traditional or classical methods in material science, which is based on the continuum mechanics. One fundamental assumption made in the finite element method is that matter in each element is homogeneous, so that all the atomistic details are neglected. This assumption works very well for the macroscopic objects, where atomistic behavior is not important, or can be interpreted by macroscopic physical quantities via statistical physics. However, continuum mechanics is insufficient at all to describe the microscopic or meso-scopic phenomenon, such as the mechanism of mass diffusion, mechanical failure, energetic stability of nano-materials, *etc.*

In the microscopic or meso-scopic world, a material should be further described at least in terms of ions, electrons, and the interactions among them. In this molecular description, the materials are discretized: each ion is represented by a spatial point, although the visualization tools often render them as a sphere, with a finite radius. The radius is pre-set according to the isolated atom with electrons around it. The chemical bonds are denoted by the lines between two interacting atoms. Similarly, the visualization tools usually render the bonds as sticks, with a finite thickness representing the electron cloud symbolically. Based on these descriptions, a theory for the interaction between atoms must be provided in order to describe how a molecule or material is formed.

1.1.1 Classical Force Field

Classical force field model describes material with the empirical potential energy, which must be parameterized. This potential energy is broken up into various terms, and each term is described by a mathematical function. In a classical force field model, there is no concept of electron, which is treated as an inseparable part of atoms. Therefore, the potential energy is merely determined by the coordinates of all the atoms in the molecule or material.

The simplest classical force field is the hard sphere potential [1],

$$E_{(\vec{r}_1, \vec{r}_2)} = \begin{cases} \infty, & |\vec{r}_1 - \vec{r}_2| < r_0 \\ 0, & |\vec{r}_1 - \vec{r}_2| \geq r_0 \end{cases} \tag{1.1}$$

where, $\vec{r}_1$ and $\vec{r}_2$ are the coordinates of two given atoms. This model works efficiently and pretty well for the materials in low density liquid or gas phase, because this model ignores all the interaction details other than the repulsion in a very short range. In another word, the atoms in this model do not interact with each other when the distance between them is greater than the critical radius, r_0, while the repulsion is too strong to allow any pair of atoms to stay closer than r_0.

For carbon and silicon materials, one of the best classical models was introduced by Tersoff and Brenner decades ago [2]. The binding energy in Tersoff-Brenner potential follows Abell-Tersoff formalism [2]:

$$E_p = \frac{1}{2} \sum_i \sum_{j \neq i} [V_R(r_{ij} - B_{ij} V_A(r_{ij})] \tag{1.2}$$

where, $V_R(r)$ and $V_A(r)$ are the repulsion and attraction terms for each pair of atoms in the materials, and B_{ij} is so-called bond-order function. This bond-order function is highly determined by the local environment of the atoms in order to represent their chemical bond nature. Under the first order approximation, this bond-order function can be written as,

$$B_{ij} \propto Z_{ij}^{-\delta} \tag{1.3}$$

in which, the factor δ is different from one case to another, and Z_{ij} is the number of bonds competing with the bond ij. For example, if the ith carbon atom has already 4

nearest neighbors, this bond-order function increases dramatically in order to prevent this carbon atom from forming the fifth bond.

Importantly, Tersoff-Brenner potential can also describe the π-bonding in carbon as well as the σ-bondings. The pioneering work on carbon nanotube [3] is one of the successful applications of this method [4, 5]. Classical potential is certainly one of the fastest simulation methods, and successfully describes material's mechanical and thermal properties. This method cannot be used to perform any optical or electronic property calculation, and it will often fail under the circumstances where the accurate calculations for chemical reactions are required. Additionally, classical potential method requires well-defined potential for all the chemical bonds. Therefore, it cannot well describe the materials which have different chemical bonding nature than the ones included in its potential energy functions.

1.1.2 Tight-Binding (TB)

Tight-binding (TB) method [6, 7] originates from one of the quantum chemistry methods, linear combination of atomic orbitals method (LCAO) [8, 9], developed for the molecules by Slater and Koster in 1954. Tight-binding theory states that the potential energy of a material or molecule consists of two parts:

$$E = E_{Ion-Ion} + E_{band} \tag{1.4}$$

where, $E_{Ion-Ion}$ is the repulsive part between ions, and E_{band} is the attractive part between electron and ion. In principle, these two parts of the potential energy are not separable. We apply Born-Oppenheimer approximation (or diabatic approximation) [10], which assumes that all the ions move slowly enough so that all the electrons reach the equilibrium at any moment. Generally, this statement is valid, because electron is so light compared to any ion. Typically, the velocity of electron is in the same order of the Fermi velocity, $v_F \approx 10^6 \ m/s$, while the velocity for ions is on the order of $10^3 m/s$. With the Born-Oppenheimer approximation, ions can be treated separately as classical particles, and electron-ion and electron-electron interactions can be calculated with quantum mechanics.

Furthermore, another foundation of tight-binding theory and LCAO is that all the electrons are tightly bounded to the ions. Even though the tight-binding theory works very well for π electrons, which are nearly free in the conjugated organic complex. Therefore, the wavefunctions of the electrons, $|\psi\rangle$, are in terms of the atomic orbitals of individual or isolated atoms.

$$|\psi\rangle = \sum_{i,\alpha} c_{i,\alpha} |\phi_{i,\alpha}\rangle \qquad (1.5)$$

where, $|\phi_{i,\alpha}\rangle$ is the αth orbital of the ith atom, and $c_{i,\alpha}$ is the corresponding coefficient. According to quantum mechanics, these wavefunctions follow the Schrödinger equation,

$$H |\psi\rangle = \epsilon_n |\psi\rangle . \qquad (1.6)$$

The simplest example is the diatomic molecule, where, $|\psi\rangle = c_1 |\phi_1\rangle + c_2 |\phi_2\rangle$. By

multiplying $\langle \phi_i |$, $(i = 1, 2)$, both sides of the Eq. 1.6, one can get an equation set as follows,

$$\begin{pmatrix} H_{11} & H_{12} \\ H_{21} & H_{22} \end{pmatrix} \begin{pmatrix} c_1 \\ c_2 \end{pmatrix} = \epsilon \begin{pmatrix} S_{11} & S_{12} \\ S_{21} & S_{22} \end{pmatrix} \begin{pmatrix} c_1 \\ c_2 \end{pmatrix} \tag{1.7}$$

in which, $H_{ij} = \langle \phi_i | H | \phi_j \rangle$, and, $S_{ij} = \langle \phi_i | \phi_j \rangle$. For non-trivial solutions, the determinant of $(H - \epsilon S)$ must be zero:

$$\begin{vmatrix} H_{11} - \epsilon S_{11} & H_{12} - \epsilon S_{12} \\ H_{21} - \epsilon S_{21} & H_{22} - \epsilon S_{22} \end{vmatrix} = 0 \tag{1.8}$$

Therefore,

$$\epsilon_\pm = \frac{(\mathcal{E}_1 + \mathcal{E}_2 - 2SV) \pm \sqrt{(\mathcal{E}_1 + \mathcal{E}_2 - 2SV)^2 - 4(1 - S^2)(\mathcal{E}_1 \mathcal{E}_2 - V^2)}}{2(1 - S^2)} \tag{1.9}$$

where, $\mathcal{E}_i = H_{ii}$ is the self-energy of the i_{th} atom, $V = H_{ij}$ is the interaction between two atomic orbitals, and the overlaping between them: $S_{ii} = 1$ and $S_{ij} = S$. With orthogonal orbital approximation, $S = 0$, one can get: $\epsilon_\pm = \bar{\mathcal{E}} \pm \sqrt{\Delta^2 + V^2}$, where, the average energy level $\bar{\mathcal{E}} = \left(\frac{\mathcal{E}_1 + \mathcal{E}_2}{2} \right)$ and the polar energy $\Delta = \left| \frac{\mathcal{E}_1 - \mathcal{E}_2}{2} \right|$. These two solutions are corresponding to the bonding state and the anti-bonding state, respectively.

From a molecule to the condense phase of material, we need to apply the periodic boundary condition (PBC) with Bloch's theory [6]:

$$\Phi_{n,\alpha}(\vec{k}, \vec{r}) = \frac{1}{\sqrt{N}} \sum_j e^{i\vec{k} \cdot \vec{R}_j} \phi_{n,\alpha}(\vec{r} - \vec{R}_j) \tag{1.10}$$

in which, $\phi_{n,\alpha}$ is the α orbital of the nth atom, $\vec{R}_j = j_1 \vec{a}_1 + j_2 \vec{a}_2 + j_3 \vec{a}_3$, is the Bravais

lattice vector, and $\vec{k}$ is the reciprocal lattice vector [6]. Overall, the molecular orbital wavefunction, $\Psi = \frac{1}{\sqrt{N}} \sum_{n,\alpha} \sum_{j} c_{n,\alpha} e^{i\vec{k}\cdot\vec{R}_j} \phi_{n,\alpha}$.

For a 1-dimensional single-orbital atomic chain, $k = \frac{j}{N} \cdot \frac{2\pi}{a}$, where a is the lattice constant, N is the number of atoms in the unit cell, and $j = 1, 2, \cdots, N$. The Schrödinger equation becomes,

$$H \sum_{j} e^{ikR_j} \phi = \epsilon(k) \sum_{j} e^{ikR_j} \phi \tag{1.11}$$

Multiplying ϕ^* in both sides, one can get the following recursive equation as follows,

$$e^{-ika} H_{j-1,j} + H_{j,j} + e^{ika} H_{j+1,j} = \epsilon(k) \left(e^{-ika} S_{j-1,j} + S_{j,j} + e^{ika} S_{j+1,j} \right) \tag{1.12}$$

For the orthogonal approximation and the nearest neighbor approximation, the solution for this atomic chain is $\epsilon(k) = \mathcal{E}_0 + 2V_0 \cos ka$, where, $\mathcal{E} = H_{j,j}$ is the self-energy, and $V_0 = H_{j\pm1,j}$ is the covalent energy [6]. For a infinite long atomic chain, $\Delta k = \frac{2\pi}{Na} \to 0$, since $N \to \infty$. Consequently, the electronic band energy becomes a continuous function of k, and this is also called energy dispersion function.

For a two dimensional lattice, such as graphene sheet [11], one will get a secular equation set as follows,

$$\begin{pmatrix} H_{AA} & H_{AB} \\ H_{BA} & H_{BB} \end{pmatrix} \begin{pmatrix} c_A \\ c_B \end{pmatrix} = \varepsilon(\vec{\mathbf{k}}) \begin{pmatrix} S_{AA} & S_{AB} \\ S_{BA} & S_{BB} \end{pmatrix} \begin{pmatrix} c_A \\ c_B \end{pmatrix} \tag{1.13}$$

in which,

$$
\begin{cases}
\begin{aligned}
H_{AA} &= H_0 + \left[e^{i\vec{k}\vec{a}_1} + e^{-i\vec{k}\vec{a}_1} + e^{i\vec{k}\vec{a}_2} \right. \\
&\quad \left. + e^{-i\vec{k}\vec{a}_2} + e^{i\vec{k}(\vec{a}_1 - \vec{a}_2)} + e^{-i\vec{k}(\vec{a}_1 - \vec{a}_2)} \right] H_2 + \cdots \\
&= H_0 + \left[2\cos\left(\tfrac{\sqrt{3}}{2} k_x a + \tfrac{1}{2} k_y a \right) + 2\cos\left(\tfrac{\sqrt{3}}{2} k_x a - \tfrac{1}{2} k_y a \right) \right. \\
&\quad \left. + 2\cos\left(k_y a \right) \right] H_2 + \cdots \\
&= H_0 + \left[4\cos\left(\tfrac{\sqrt{3}}{2} k_x a \right) \cos\left(\tfrac{1}{2} k_y a \right) + 2\cos\left(k_y a \right) \right] H_2 + \cdots \\
H_{AB} &= \left[e^{i\frac{1}{3}\vec{k}(\vec{a}_1 + \vec{a}_2)} + e^{-i\frac{1}{3}\vec{k}(\vec{a}_1 - 2\vec{a}_2)} + e^{-i\frac{1}{3}\vec{k}(2\vec{a}_1 - \vec{a}_2)} \right] H_1 + \cdots \\
&= \left[e^{-i\frac{\sqrt{3}}{3} k_x a} + 2\cos\left(\tfrac{1}{2} k_y a \right) e^{i\frac{\sqrt{3}}{6} k_x a} \right] H_1 + \cdots
\end{aligned}
\end{cases}
\tag{1.14}
$$

with H_0 is the *self energy*, H_n is the interaction energy between the nth-nearest-neighbors (*e.g.*, H_1 is the interaction energy between a pair of atoms which are the nearest neighbors). For the orthogonal approximation, one can the electronic bands as follows,

$$
\begin{aligned}
\varepsilon(\vec{k}) &= H_0 + \left[4\cos\left(\frac{\sqrt{3}}{2} k_x a \right) \cos\left(\frac{1}{2} k_y a \right) + 2\cos\left(k_y a \right) \right] H_2 \\
&\quad \pm \left[1 + 4\cos^2\left(\frac{1}{2} k_y a \right) + 4\cos\left(\frac{1}{2} k_y a \right) \cos\left(\frac{\sqrt{3}}{2} k_x a \right) \right]^{\frac{1}{2}} H_1 + \cdots
\end{aligned}
\tag{1.15}
$$

This simple analytical solution shows the band structure of graphene successfully, and also gives clear classification and explanation of the interesting electronic properties of single-walled carbon nanotube [3, 5]. The essential parts of the tight-binding models are the Hamiltonian (H_{ij}) and the overlap (S_{ij}) matrix, and the number of the orbitals considered. Depending on the calculation, one can choose different

tight-binding models from orthogonal single orbital nearest neighbor interaction to non-orthogonal multiple orbital long range interaction models. The matrix elements of H_{ij} and S_{ij} can be parameterized by the empirical data, and/or from the higher level computations, *i.e.* density functional theory (DFT) in the later chapter. Density functional based tight-binding (DFTB) introduced by Porezag and his colleagues [12] is parameterized via the DFT method. Trocadero [13, 7] is one of the simulation packages that employs DFTB.

Tight-binding method is one of the cheapest methods based on quantum mechanics, and it works fairly well for covalent systems, especially the organic molecules and semiconductors with elements from the group IV in the periodic table: including carbon [14] and silicon [15]. The biggest drawback for tight-binding method is that it does not describe the chemical bonds as well as the covalent bonds, so that one should turn to other methods when the materials have noncovalent bonds.

1.1.3 Semi-Empirical

Before we move to the first principle method, we want to introduce another important transition method, which lies between expensive first principle (or *ab initio*) method and empirical data dependent classical potential method. This method adapts one of the first principle method, Hartree-Fock's framework, and it is so-called semi-empirical method. Therefore, the semi-empirical method does not have any preference

for the elements or certain molecule/material in principle, which gives the computer simulation much more freedom. Nevertheless, because the semi-empirical methods still require empirical data for parameterization, their performance and availability are dependent on whether and how the parameterization is deployed.

Semi-empirical methods were first developed by J. Pople in 1960's, including complete neglect of differential overlap (CNDO), intermediate neglect of differential overlap (INDO), and neglect of diatomic differential overlap (NDDO) [16]. Lately, due to the performance and accuracy, two relatively new semi-empirical methods become popular, Austin model 1 (AM1) [17] and parameterized model 3 (PM3) [18], which are developed lately by M. J. S. Dewar *et al.*, and J. J. P. Stewart, respectively.

According to the Pauli exclusion principle and Hartree-Fock theory, the N-electron wavefunction $|\Psi\rangle = |\psi_1\psi_2\cdots\psi_N\rangle$ can be written as a Slater determinant,

$$|\Psi\rangle = (N!)^{-1/2} \begin{vmatrix} \psi_1(\vec{r}_1) & \psi_2(\vec{r}_1) & \cdots & \psi_N(\vec{r}_1) \\ \psi_1(\vec{r}_2) & \psi_2(\vec{r}_2) & \cdots & \psi_N(\vec{r}_2) \\ \cdots & \cdots & \cdots & \cdots \\ \psi_1(\vec{r}_N) & \psi_2(\vec{r}_N) & \cdots & \psi_N(\vec{r}_N) \end{vmatrix} \qquad (1.16)$$

where, each single electron wavefunction ψ_i is an eigenfunction of the following Hamiltonian:

$$H^{HF} = -\frac{1}{2}\nabla^2 - \sum_{m=1}^{M} \frac{Z_m}{R_m} + V^{HF}(\rho) \qquad (1.17)$$

One may notice that this Hamiltonian is a function of the electron density, $\rho = \sum_i \langle\psi_i|\psi_i\rangle$. In Hartree-Fock method, this chicken-and-egg problem is solved by Hartree-Fock self-consistent field (SCF) scheme. Instead of pure HF-SCF, semi-empirical

methods employ parameterization and a variety of approximations to speed up this procedure.

The parameterization in semi-empirical methods can be based on the *ab initio* as well as the experimental data, and both AM1 and PM3 choose the later. Nevertheless, semi-empirical methods still perform the self-consistent calculation for the electron density and Hamiltonian. Consequently, semi-empirical methods describe the far-equilibrium conditions better than tight-binding method usually, such as chemical bond association/dissociation. In this thesis, two softwares are used to perform the AM1 semi-empirical computations, Gaussian [19] and Dynamo [20].

1.1.4 *Ab Initio*

Previously, we already mentioned one of the *ab initio* methods, Hartree-Fock method. Because all these methods are solely based on the theories themselves, the *ab initio* methods are often called *first principle* methods.

The most successful and frequently used *ab initio* method is the density functional theory (DFT) method. Density functional theory was based on the Hohenberg-Kohn theorems and the Kohn-Sham equations [21]. Hohenberg and Kohn first proved that both the density and wavefunction of an electron gas are existing and non-degenerate when the system reaches its ground state. The second theorem of the Hohenberg-Kohn theory is that there exists an universal exchange-correlation functional of the

electron density, $E_{xc}[\rho]$. The ground state electron density minimizes the electronic energy,

$$E[\rho] = -\frac{1}{2} \int d\vec{r}\Psi^*\nabla^2\Psi + \frac{1}{2} \int d\vec{r} \int d\vec{r}'\frac{\rho(\vec{r})\rho(\vec{r}')}{|\vec{r}-\vec{r}'|} + \int d\vec{r}V^{ext.}\rho(\vec{r}) + E_{xc}[\rho] \quad (1.18)$$

where, ρ is electron density, and $V^{ext.}$ is external potential.

Therefore, the key issues for density functional theory are identifying the exact E_{xc} and solving the Schrödinger equation. Kohn and Sham provided a recipe to solve the many particle Schrödinger equation with single electron approximation [21]. However, a variety of exchange-correlation functionals are proposed. There are two groups of functionals in DFT method, local density approximation (LDA) and generalized gradient approximation (GGA). In local density approximation, the exchange-correlation functional is only in terms of the local density of the electrons, while the generalized gradient approximation includes the gradient of electron density. The exchange-correlation functional in LDA is parameterized with high accuracy quantum Monte Carlo calculations by Ceperley and Alder [22], and later improved by Vosko, Wilk, and Nusair (VWN) [23].

Local density approximation works well and relatively efficiently, but it usually overestimates the interaction and underestimates the bond length. Due to the simpler mathematical form of the LDA functionals, local density approximation can be enhanced by consideration of higher order terms, *i.e.* GGA. There are quite a lot GGA functionals available, including Perdew 86 (P86) [24], Becke 95 (B95) [25],

Perdew-Burke-Ernzerhof (PBE) [26], and Lee-Yang-Parr (LYP) [27]. Furthermore, Becke developed the so-called hybrid functionals [28], which include both LDA and GGA functionals with different parameterizations. Since this hybrid DFT method works extremely well in most systems, it is widely used and is becoming more and more popular.

The choice of the functional directly balances the efficiency and accuracy of the computations. The way to construct the wavefunction is quite important. Conventionally, a wavefunction can be constructed from either localized atomic wavefunctions or plane waves. According to the Fourier theory, these two methods are identical in principle. In reality, one should construct the wavefunction from a finite number of primitive mathematical functions. For different circumstances, it would be ideal to choose the right construction. For example, the plane waves used in Vienna Ab-initio Simulation Package (VASP) more naturally represent the periodic systems and delocalized electrons, while the Gaussian shape localized functions used in Gaussian [19] are much more efficient to describe localized atomic orbitals than the plane waves. Since Gaussian orbitals have difficulty to descrbe the singularities near atomic nuclei, a new wavefunction basis set, linear combination of numerical atomic orbitals (LCAO), is becoming more and more popular for DFT method. SIESTA [29] is one of the *ab initio* simulation packages using LCAO.

Another important issue for the *ab initio* calculation is the pseudopotential. Al-

though Kohn-Sham theory approximatively solves the many-particle problem of the electron gas, the calculation for the self-consistent iteration is still very costly. It becomes more and more severe when we are trying to deal with elements with large atomic number, such as Au. The all-electron calculation becomes very demanding, but most of the electrons in the inner shells, so-called core electrons, are not involved forming chemical bonds and remain intact. Pseudopotential is one of the solutions for this problem. In this approximation, one replaces all the core electrons by a precalculated potential called pseudopotential within the cutoff radius. During the run-time calculations, these core electrons are treated as a fixed external potential. Notably, it's quite important to choose a right pseudopotential for different systems, because there is no universal choice for all the calculations. Without careful consideration and testing, one may end up either wasting computational time on core electrons or losing accuracy by freezing valence electrons, especially, for the first two rows of elements in the periodic table.

In *ab initio* calculations, the electron density or wavefunction is computed either in a fine grid of the real-space of the computational unit cell or within a cut-off value in the momentum-space. Consequently, how to choose a suitable grid or cut-off momentum can also influence the accuracy or efficiency of the simulations significantly.

1.2 Computational Molecular Simulations

With either one or several different theoretical models in the last section, we are able to compute the static properties of given molecules or materials. In other words, one can obtain a stable structure as an output by minimizing the energy of the given molecule or material. This type of calculation is called geometry relaxation or optimization. However, one may have no information yet on any of the thermodynamic properties, such as the stability of a given material under the temperature, T, and the pressure, P. In this section, how to relate the individual molecule or the computational unit cell to the macroscopic material with 10^{23} molecules/atoms will be shown. Two elementary (deterministic and stochastic) molecular simulation methodologies will be covered herein.

1.2.1 Molecular Dynamics Simulation (MD)

Molecular dynamics simulation can describe the molecules or materials with either classical mechanics or quantum mechanics, or both. Due to the complexity and difficulty of solving the time-dependent Schrödinger equation in quantum mechanics, only classical molecular dynamics is widely used in molecular dynamics simulations. Therefore, we focus on the classical molecular dynamics simulation.

Although the force or interaction between nuclei can be computed with the models

described in the last section, Newtonian classical mechanics is used to describe the evolution of N atoms in materials.

$$\frac{d\vec{p}_i}{dt} = \frac{\partial E(\vec{r}_1, \vec{r}_2, \cdots, \vec{r}_N)}{\partial \vec{r}_i} \tag{1.19}$$

and

$$m_i \frac{d\vec{r}_i}{dt} = \vec{p}_i \tag{1.20}$$

in which, E is the potential energy, $\vec{r}_i$ and $\vec{p}_i$ are the coordinate and momentum of the ith atom, respectively. The trajectory of all the atoms virtually demonstrates and predicts the dynamic behavior of the material. The evolutions of the coordinate and momentum are calculated with the finite difference method. Therefore, for each time step, Δt, the coordinate and momentum update once according to Newton's laws. The velocity Verlet method [30] is one of the most efficient algorithms for updating the velocities and coordinates. Instead of direct motion integration, the velocity Verlet approach updates the velocity and coordinate with more than just one step in advance. The formula are shown below,

$$\vec{r}_i(t + \Delta t) = \vec{r}_i(t) + \vec{v}_i\left(t + \frac{1}{2}\Delta t\right)\Delta t \tag{1.21}$$

and

$$\vec{v}_i\left(t + \frac{1}{2}\Delta t\right) = \vec{v}_i\left(t - \frac{1}{2}\Delta t\right) + \vec{a}_i(t)\Delta t \tag{1.22}$$

According to statistical physics, there are three principal thermodynamics ensembles [31, 32]: microcanonical ensemble, canonical ensemble, and grand canonical ensemble. Correspondingly, there are three different molecular dynamics simulations: microcanonical simulation, canonical simulation, and grand canonical simulation. More specifically, in microcanonical simulations, the number of the atoms, N, the volume of the material, V, and the total energy of the systems, $E = E_k + E_p$, are not variables. Conventionally, it is named NVE simulation. In canonical simulation, instead of the total energy, the temperature of the system T remains constant, and it is named NVT simulation. Finally, grand canonical allows the number of the atoms in the system to change, while simulation temperature and volume are constants.

Theoretically, molecular simulation is a deterministic simulation, but the simulation contains stochastic processes in reality. The simulation randomly assigns each atom with an initial velocity, while the velocities of all the atoms follow Boltzmann's distribution. For different simulations, either the total energy or temperature converges to its preset value. The procedure and the bath (energy, temperature, or particle bath) to control the thermodynamics physical quantities is called thermostat. One of the widely used thermostat schemes is called the Nose-Hoover thermostat [33].

1.2.2 Monte Carlo Simulation (MC)

In contrast to the deterministic molecular dynamics simulation, Monte Carlo simulation is categorized as a stochastic simulation. The atoms in the simulation do not follow Newtonian mechanics. Instead, the system randomly moves the atoms in the phase-space, either one atom or all atoms at each step. With the models provided in the last section, system computes the energy of each configuration. According to the Ergodic hypothesis, the system will visit all the positions in the phase-space over long periods of time. Consequently, the thermodynamic average of the physical quantity is approaching the true value.

However, Monte Carlo becomes impractical because it takes an infinite length of time to simulate a true "long" time. In 1953, Metropolis *et al.* [34] proposed an approach for Monte Carlo methods, which makes Monte Carlo methods powerful in practical applications. In this approach, a weight is assigned to each Monte Carlo snapshot or ensemble, $\exp\left(-E/k_BT\right)$, and each move is also adjusted by this weight. For example, the energy change for one move is ΔE, the probability to accept this move is calculated as $\min\left[1, \exp(-\Delta E/k_BT)\right]$. When energy is going upward, the move has much more chance to be "rejected" than the move with a smaller energy increase, while the moves with the energy going downhill are always accepted. Consequently, the system can visit the phase-space much more efficiently. Even though the

system may not really visit the high energy positions, this Boltzmann weight ensures that the average is still quite accurate because of their negligible weights.

Because many dynamic details are not calculated in Monte Carlo method, this method cannot tell us things like how the defect is generated in the material, or how chemical bonds are dissociated. Nevertheless, because of this, Monte Carlo is very efficient to calculate the thermodynamic quantities such as the Gibbs free energy. For example, Monte Carlo can easily give us how several defects are going to migrate statistically in the material, while one should run molecular dynamics simulations numerous times over a fairly long time in order to get an accurate statistics.

Chapter 2

Mass Transport through Graphene Layer

2.1 Introduction

Interstitial carbon is one of the most important defects in the carbon materials. The formation and the diffusion of the interstitials has been investigated from both experimental [35] and theoretical perspectives [36, 37, 38, 39, 40, 41] for decades, and been believed to have a significant barrier in the basal direction, which is larger than $5\ eV$ [35, 41].

Recently, a significant shrinkage of perfectly sealed multiple layered carbon onions [42, 43] is reported by Banhart and his colleagues. Furthermore, different groups independently observed diameter reduction of the seamless multi-walled carbon nanotubes [44, 45, 46], while the tubes retain their perfection [47, 48]. These experiments indicate that there must be a diffusion channel for carbon atoms to penetrate the seamless graphene walls, and it seems that this contradicts to the experiments in the literatures and cannot be reconciled by any of the existing theoretical models.

Sigle and Redlich [49] proposed an interesting phenomenological diffusion mech-

anism from a statistical perspective, which is irradiation-induced diffusion of the vacancies from the outermost shell towards the core of the carbon onion. Obviously, it is not convincing enough to conclude this problem without further atomistic understanding. Additionally, Banhart *et al.* investigated and exposed some details of the migration of metal atoms through carbon onions [50], although the atomistic mechanism of this diffusion remains veiled.

In this chapter, we will begin with the experiment of a growing fullerene inside of the larger fullerenes, which is a reverse process of the carbon onion shrinkage. We propose a diffusion mechanism of C_2 molecules instead of single carbon interstitials. The diffusion can be decomposed into three stages: i) absorption of C_2 molecule and forming addimer on graphene lattice; ii) addimer flipping from one side of the graphene to the other side; iii) dissociation of the addimer. The overall transition barrier, computed with density functional theory (DFT) method, is surprisingly lower than the barrier for single interstitial or vacancy diffusion. The diffusion flux is calculated accordingly, and is consistent with the experiment.

2.2 Experiment

The experiments are conducted inside a high-resolution transmission electron microscope (HRTEM) equipped with a nanofactory TEM-STM (scanning tunneling microscopy) platform, enabling *in situ* manipulation of individual carbon nanotubes.

Individual MWCNT glued to an *Au* rod is connected to the STM probe by *in situ* deposition of amorphous carbon. A detailed experimental procedure is described in Ref. [51]. Once a connection is established, a high bias voltage is applied to Joule heat the nanotube. The nanotube is Joule heated to about $2000°C$ at high bias voltages [51, 52, 53]. At such a high temperature, a shell-by-shell self-templated growth of fullerene takes place in the inner chamber of the MWCNT.

The first fullerene in Fig. 2.1 (a-e) is grown due to the breakage and wrap-up of the innermost wall of the MWCNT. Then, a small island grows on the inner surface of the first fullerene (f-h), and the island extends until the second fullerene is closed. Notably, there is a spacing between the first and the second fullerene (i-j). Following the same fashion as the growth of the second fullerene, the third fullerene is grown on the inner surface of the second fullerene (k-o). The same spacing is kept between the third and the second fullerene as well.

Initially, the carbon source comes from the residue of the broken carbon nanotube walls and the carbon gas in the inner chamber of the MWCNT. The growth of the second and the third fullerenes in the inner surface of the outermost fullerene is surprising and entirely unexpected, since carbon atoms have to penetrate the enclosed perfect fullerene to grow the second fullerene.
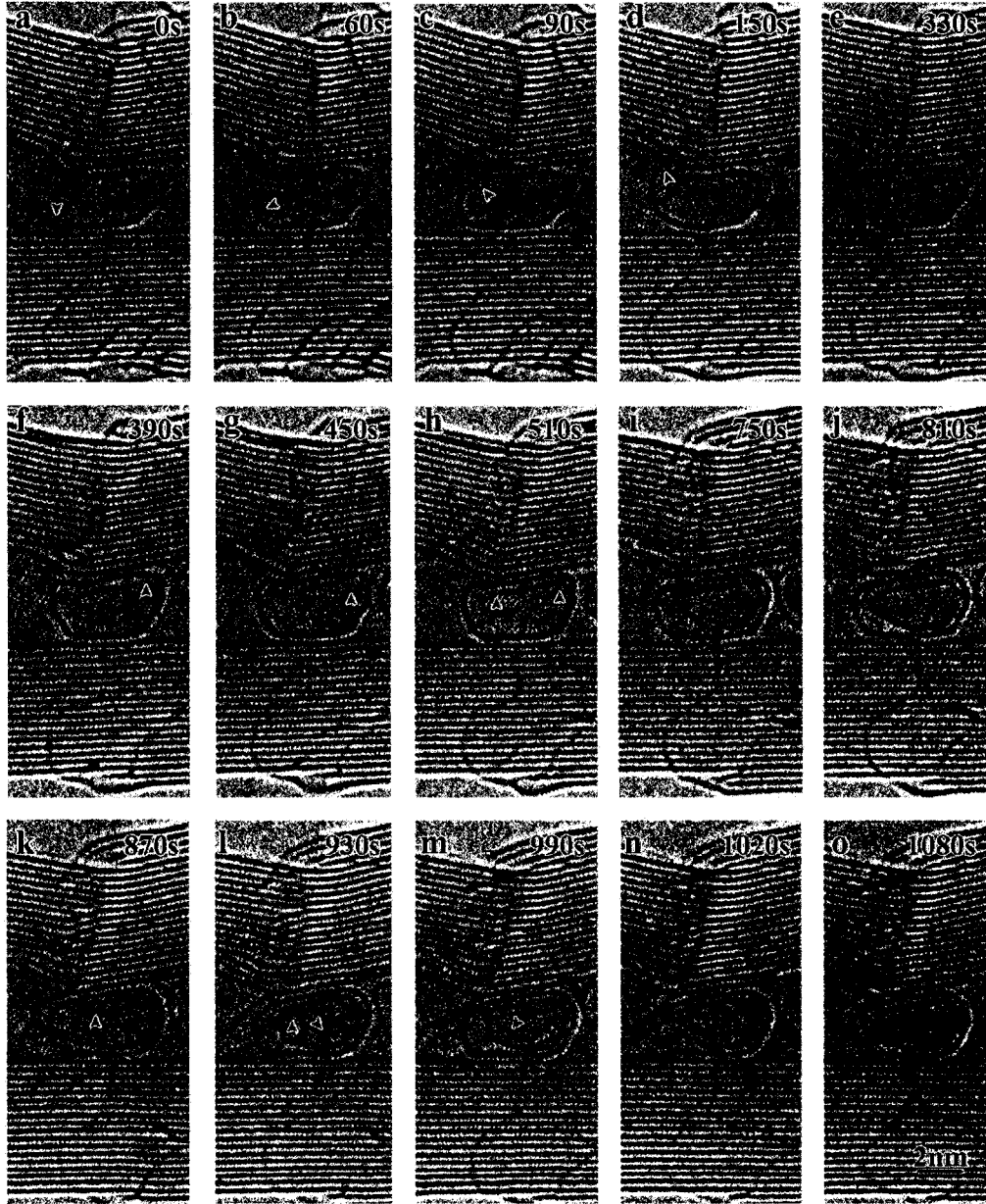
Figure 2.1 Sequential HRTEM images showing the self-templated growth of three consecutive fullerenes. The nanotube is Joule heated to $\sim 2000°C$ by applying a bias voltage of $2\ V$. The time elapse are marked, and the arrowheads point out the growth front of the fullerenes.

2.3 Direct Penetration

Before we explore new mechanism of carbon diffusion through the hexagonal carbon network, let us first look at the most intuitive mechanism, direct penetration. In this mechanism, carbon atoms penetrate through the center of the polygons, *i.e.* hexagon for a perfect graphene lattice. We employed the density functional based tight-binding molecular dynamic (DFTB-MD) simulations for our investigations.

In Fig. 2.2 (a), we schematically show how carbon atoms will shoot towards the lattice in our calculations. Due to the high reactivity of the atomic form, carbon tends to form the C_2 molecular form, which is a relatively more stable gas phase than carbon plasma. Therefore, we only consider C_2 molecule in our simulations. Initially, we keep the carbon-carbon double bond in C_2 normal to the plane of the graphene lattice, and aim the C_2 to the center of the polygon which the C_2 molecule is attempting to penetrate. The C_2 molecule is given an initial shooting momentum normal to the graphene plane before we start the micro-canonical MD simulations. Due to the radicals, C_2 molecule senses the carbon atoms in the lattice and tends to form chemical bonds with them. Consequently, C_2 will be chemically absorbed by the graphene layer, until the shooting velocity of the C_2 molecule is greater than the critical velocity, the minimum velocity for C_2 molecule to go through. The corresponding kinetic energy, $E_{threshold}$ for one C_2 molecule to physically penetrate a graphene layer through a hexagon is around 38 eV.
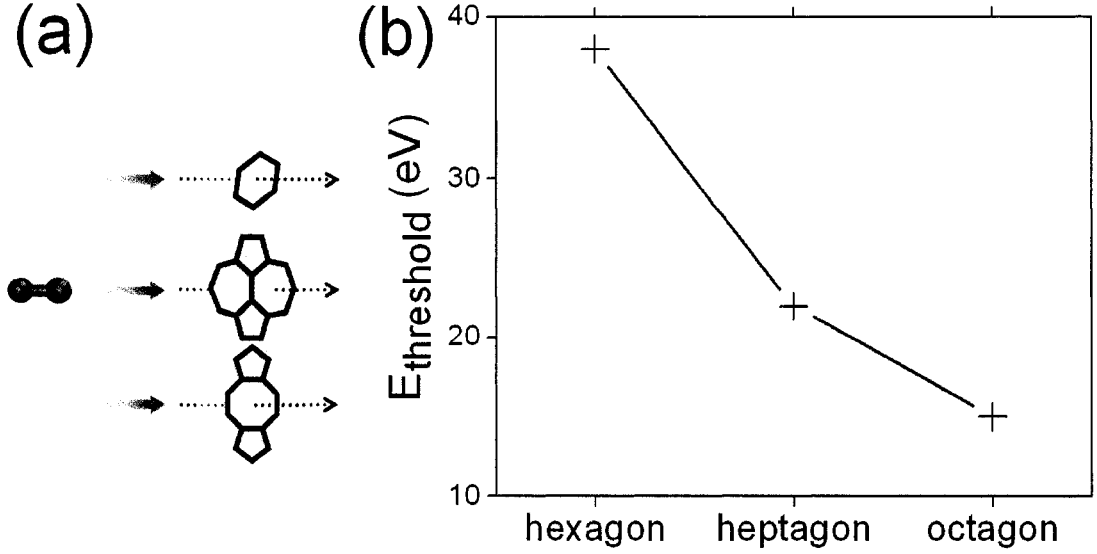
Figure 2.2 Direct penetration through carbon polygons. (a) Schematic for shooting C_2 molecule; (b) the threshold kinetic energies for C_2 molecule to penetrate different polygons.

Certainly, one can lower this threshold energy by replacing the target from hexagon to larger polygons, *i.e.* enlarging the "holes" in the graphene lattice. In our investigations, we try two other polygons, namely, heptagon and octagon. Threshold kinetic energies for different polygons are plotted in Fig. 2.2 (b). From this figure, one can see that the threshold kinetic energy for an octagon is still more than 15 eV, which is not easy for C_2 molecule to attain in the ambient conditions. Additionally, a larger "hole" on graphene will be quickly annealed to smaller holes [54]. Therefore, the physical penetration can not provide a sufficient diffusion channel in the experiments mentioned earlier, and new mechanisms need to be explored.

2.4 Flip through Graphene as Addimer

2.4.1 Addimer on Graphene Patch

Because of the high reactivity of a single interstitial carbon atom, carbon atoms are required to overcome a significantly high diffusion barrier [35, 36, 38, 41]. In contrast, in the C_2 molecular form carbon has much fewer dangling bonds than in the atomic form. Furthermore, due to the low concentration of the interstitial carbon in the graphite, it is usually difficult to form C_2 molecules. In the experiments we introduced earlier of the chapter, especially, Huang's experiment, the concentration of the free carbon gas is high enough to form C_2 molecules. Therefore, it is more reasonable to discuss the diffusion of C_2 molecules rather than the atomic form. Whether and how C_2 molecules diffuse through the graphene layer are investigated through atomistic simulations in this chapter.

In the first order approximation, the graphene layer can be treated as a hexagonal finite-sized graphene patch, such as the coronene ($C_{24}H_{12}$). It has been reported that C_2 molecule can be easily absorbed chemically by the graphene layers or the side walls of CNT and form addimer [55, 56]. In Fig. 2.3 (b), we show two different stable addimer structures: i) horizontal addimer (A_h); ii) vertical addimer (A_v). In both cases, the graphene patch is bended severely.

In order to better represent the infinite graphene layer with a patch, we freeze
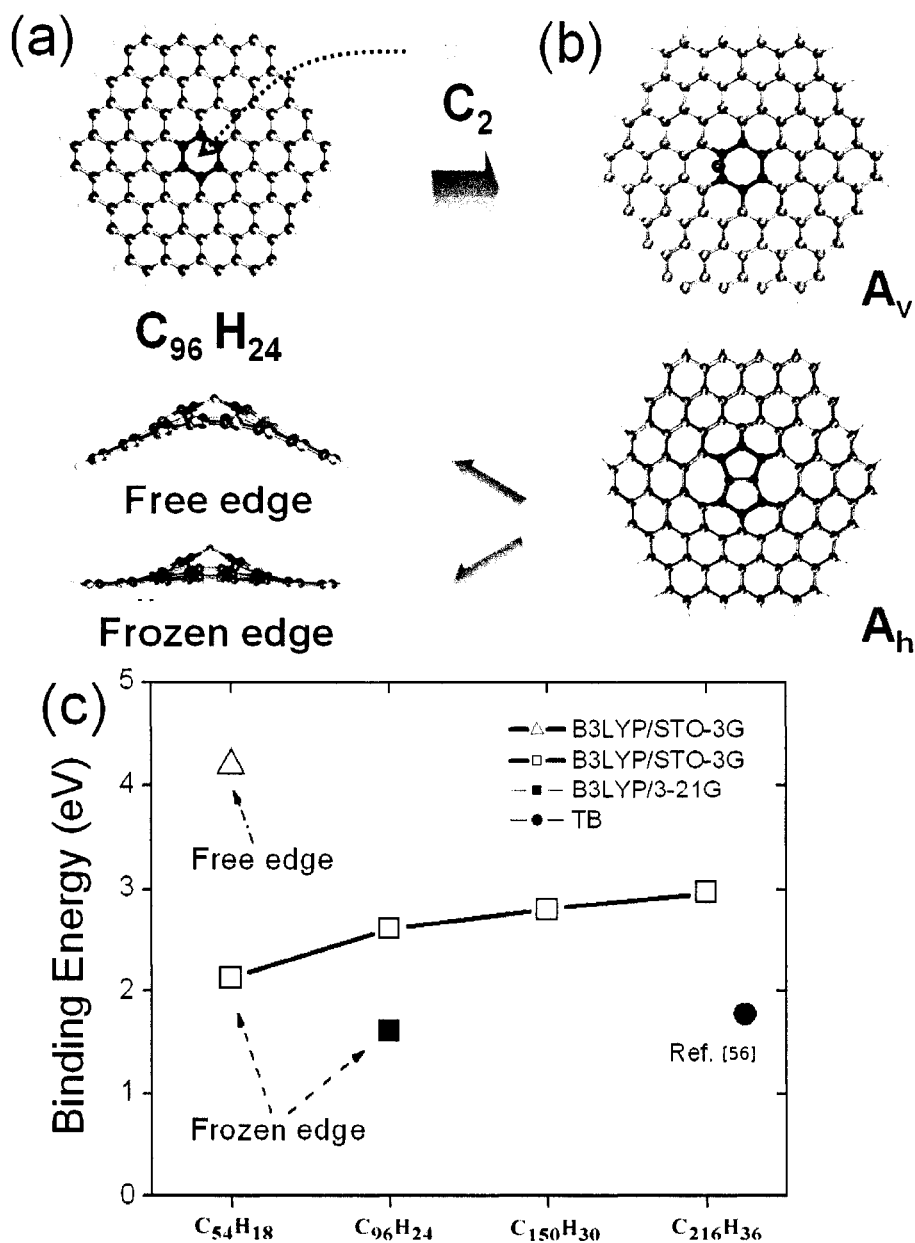
Figure 2.3 Graphene patch model. (a) Circum-circumcoronene; (b) two stable addimers: vertical addimer A_v, horizontal addimer A_h; (c) patch size dependent binding energy of A_h.

the hydrogen atoms at the edge of the fully relaxed graphene patch. The extra stress introduced by this constraint can be depressed by choosing a larger patch, such as $C_{96}H_{24}$ (circum-circumcoronene) shown in Fig. 2.3 (a). In Fig. 2.3 (b), we show the side view of an A_h addimer formed on $C_{96}H_{24}$ with frozen edge. One can see that the carbon plane is almost flat near the edge where the ripples exist for smaller patches. Moreover, the formation energy of A_h addimer (E_{add}) versus the size of graphene patch is plotted in Fig. 2.3 (c) with hollow squares. The convergence of the formation energy indicates that circum-circumcoronene is sufficiently large in our calculations. Therefore, we replace the infinite graphene by this $C_{96}H_{24}$ patch as our theoretical model, hereafter.

For the purpose of maintaining the consistency and achieving as high accuracy as we can afford, we conducted all the relaxation and saddle point searching with one software package, Gaussian [19], from now on. We employed the functional density theory method with the generalized gradient approximation (GGA) with Becke's [28] three-parameter hybrid functional in conjunction with the exchange-correlation functional of Lee, Yang, and Parr [27] (B3LYP). In addition, the STO-3G Gaussian-type basis set is used for E_{add} convergence study, and a larger basis set 3-21G is used for the rest calculations, including transition state searching. As a result, the binding energy of the A_h addimer on the circum-circumcoronene patch calculated with 3-21G basis set is 1.7 eV, which is in a good agreement to the value reported by Sternberg

et al. [56].

2.4.2   Local Buckled Plate Model

If two carbon atoms are added at the center of the patch, the circum-circumcoronene changes its shape from a plate to a hat, with a hump at the center. Naively, one can push this hump from one side of the graphene patch to the other by flattening the "hat". The energy barrier for this transition path is extremely high, which is 7.2 *eV*. Obviously, this ad-dimmer is very unlikely to flip over the graphene plane through this mechanism.

We revisit this buckled graphene patch carefully. This graphene patch is buckled in one direction much more significantly than the other direction. In material science, this addimer can be also categorized as a dislocation dipole, which consists of two dislocations face-to-face. In the direction perpendicular to the extra line, the graphene patch is highly buckled, the tiny extra line with these two absorbed carbon atoms is out of the graphene plane. This buckled plate is analogous to the Euler plate [57], if we ignore the buckling in the other direction. Since we freeze the edge of the plane, the boundary condition of this Euler plate is referred to as a hinged boundary condition [57]. According to Euler buckling theory, the solutions of the buckled plate are series of sinusoid functions:

$$f_n(x) = \sin\left(\frac{n\pi}{l}x\right) \tag{2.1}$$

where, $f_n(x)$ is the nth deflection function of the plate, and l is the length of the plate. Assuming only elastic deformation in the plate, we can directly relate the strain energy to the shape of the plate in the continuum approximation. Therefore, the strain energy, $E_n \propto n^2$.

Although there are infinite numbers of Euler buckling modes, only the first solution of the Euler buckling equation is stable, which is the bump in the circum-circumcoronene. All higher order buckling modes are saddle points. Any infinitesimal deviation from these modes will cause the energy of the plate to decrease, and eventually transform the plate to the first order mode.

Turning back to the flipping problem of the addimer on the graphenen patch, all these Euler buckling modes are just the transition states of the flipping. Therefore, the lowest energy transition state (TS) is the second order buckling mode, which has only one node between two ends. The geometry of this TS is like an "S" shown in Fig. 2.4(a). With this guess, we perform the saddle point search in Gaussian, and confirm that it is one of the transition states. The corresponding energy barrier for this transition path, $E_s = E_{TS_s} - E_{V_h}$, is only 1.0 eV. The surprisingly low barrier is because this diffusion process does not involve any chemical bond breaking. Fig. 2.4 (b), the schematics shows this diffusion path, with the analogy to the Euler plate. The
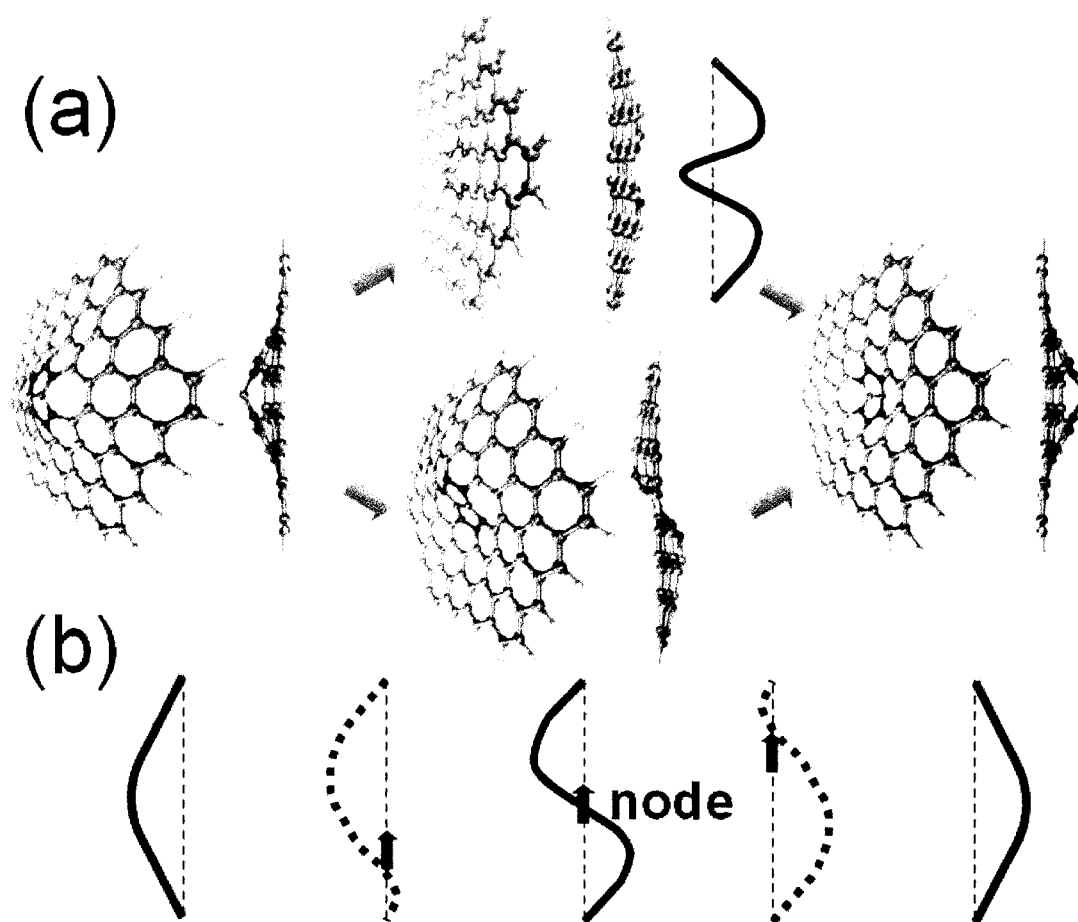
Figure 2.4   Diffusion paths for a C_2 molecule to flip from one side of the circum-circumcoronene to the other side. (a) The ball-and-stick model for the initial, transition, and final states of this diffusion path. (b) The schematic diagram for the transition path via the "S" shape transition state.

dash line is representing the intermediate configuration, which has a node between two ends as well. The node appears from one end, and moves to and disappears at the other end. This process is also very similar to acoustic wave propagation. Therefore, this process can be coupled with the acoustic mode of the graphene layer's thermal vibration, which can be clearly seen in the classical potential MD simulation of a huge graphene layer (C_{3750}) with addimers, shown in Fig. 2.6 (b).

Similarly, we predict the third order buckling mode to be the next lowest TS. This buckling mode has two nodes between two ends, and the geometry of this transition state is like an "M" shown in Fig. 2.4. Because the energies of the addimer and the TS can be approximately described as the energies of the buckling modes, $E_n \propto n^2$, this barrier can be estimated as, $(E_M - E_{ad}) = \frac{(3^2-1^2)}{(2^2-1^2)} (E_S - E_{ad}) = 2.7 \; eV$. The actual computed barrier for this transition path is 2.2 eV, and is surprisingly in agreement with our expectation. This difference is due to the complexity of the actual boundary condition, which is not just hinged plate. The transition state energy increases parabolically while the order of buckling mode is increasing. Theoretically, the flattening of the addimer can be referred to the ∞^{th} order mode, although the energy cannot be estimated in this way. In any case, the diffusion barriers for all other modes are much higher than the first two paths. Consequently, they can not make a sufficient contribution to carbon diffusion.
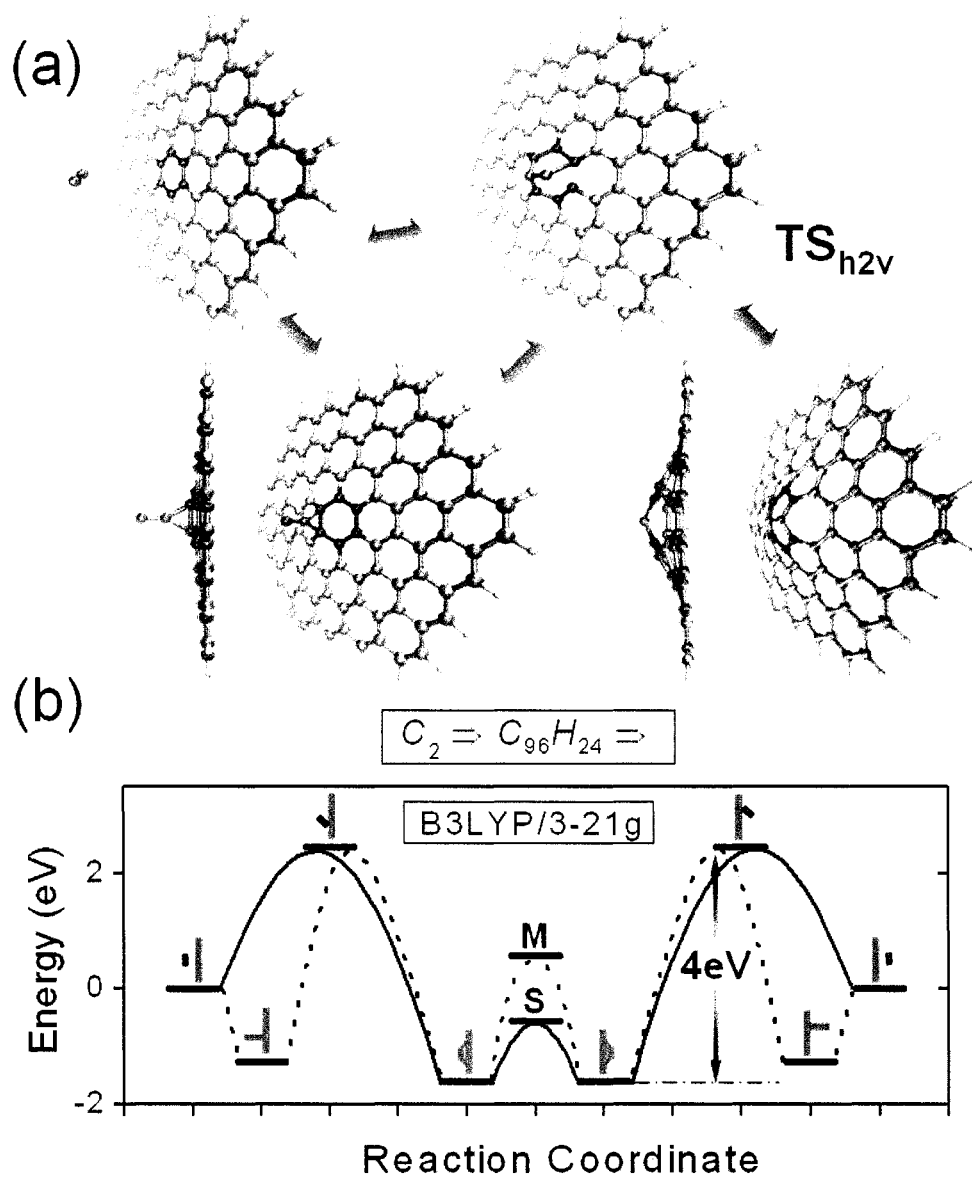
Figure 2.5 C_2 absorption and dissociation. (a) The ball-and-stick model for the C_2 absorption and dissociation processes. (b) The overall reaction coordinate for the C_2 diffusion from the gas phase to addimer, and back to gas phase.

2.4.3   MD simulation

In order to further confirm the transition state calculations, we again perform DFTB-MD simulations. During the simulations, we keep the hydrogen atoms frozen while the simulation temperature is 2000 K. We observed addimer flipping through $C_{96}H_{24}$, circum-circumcoronene after 2 ps. Clearly, we can see the addimer is following the "S" shape transition path, which has the lowest energy barrier. The snapshot of the transition state from the simulation is shown in Fig. 2.6 (a).

2.5   Diffusion Coefficient

After we locate all the possible transition path for the addimer to flip from one side of the graphene plane to the other side, we try to evaluate the diffusion coefficient of our mechanism and compare with our experiment in this section.

Although the energy barrier for addimer to flip from one side of the graphene layer to the other is surprisingly low, this barrier is not for the whole diffusion process. In order to penetrate the graphene layer, the C_2 molecule must escape from the carbon lattice and return to the gas phase. This process is similar to the "fragmentation" of the bucky ball [58, 59]. Compared to taking a C_2 away from the perfect sidewall of a C_{60}, which requires around 12 eV [58], dissociation of the inserted C_2 from an addimer has a much smaller activation barrier ($\sim$ 4 eV). This is because that
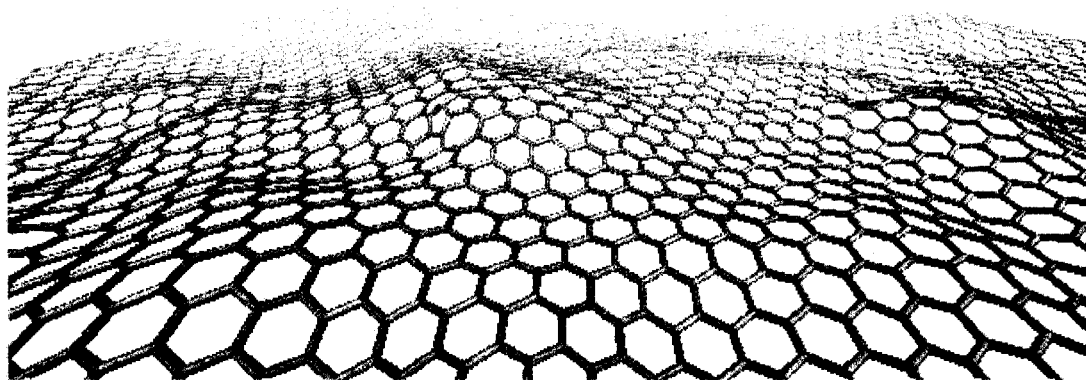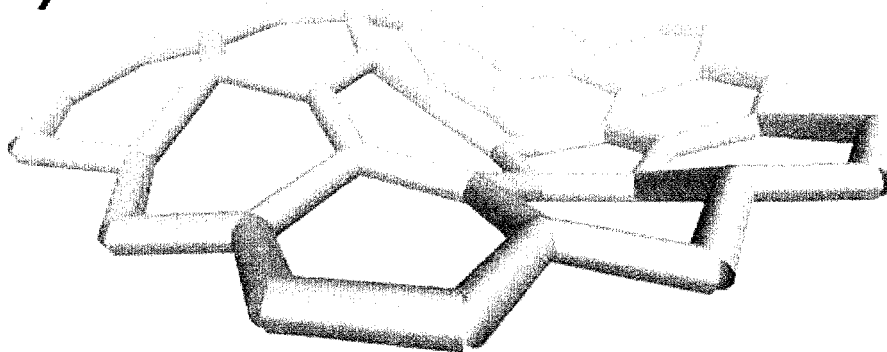
Figure 2.6 Molecular dynamics simulations. (a) Classical potential MD simulation for five addimers on C_{3750}. (b) Snapshot of the "S" shape transition state from a tight-binding MD simulation of $C_{96}H_{24}$. Only the core of the circum-circumcoronene is shown, while hydrogen and the outermost carbon are not.

the carbon network of an addimer has two adjacent pentagons violating the isolated pentagon rule (IPR) [60], and the carbon layer becomes perfect after releasing a C_2. This C_2 dissociation is the reversed process of the formation of addimer, which was briefly discussed in Ref. [56]. A_h can be formed or dissociated directly or through forming A_v, because two processes share the same transition state (TS_{h2v}), shown in Fig. 2.5.

By considering both the flipping of the addimer and the dissociation of the addimer from the graphene, we put all the favorable meta-stable structures and transition states together and show in Fig. 2.5. One can see the bottleneck of the whole diffusion process is the direct dissociation of A_h (or transformation between A_h and A_v), and the overall activation barrier is 4.1 eV. The interstitial diffusion coefficient can be evaluated by the following formula, $D = 1/2 \, v \, a^2 \exp(-E_b/k_B T)$ [61], where v is the characteristic frequency ($\sim 10^{12} s^{-1}$), a is the lattice constant, E_b is the diffusion barrier, and k_B is the Boltzmann's coefficient. Consequently, the diffusion flux of the C_2 gas through a single graphene layer at 2000 K, $J = -D \, dC/dz \sim 10^{16} s^{-1} cm^{-2}$, assuming the concentration at one side is zero and the other side is one C_2 above every five hexagons. In this case, it takes 0.2 s for the carbon atoms which are required to grow a full layer inside a fullerene to go through.

2.6 Conclusion

Carbon penetration through graphene layer in the C_2 molecular form provides a new diffusion route for mass transport in various carbon nano-structures, including fullerenes, carbon onions, and carbon nanotubes. DFT calculations show that an addimer can flip from one side to the other without breaking any chemical bond, and the activation barrier is only as low as $1\ eV$. The bottleneck of the whole diffusion process is to dissociate the inserted C_2 from the graphene layer, and the overall energy barrier is around $4\ eV$, which is much lower than any other known diffusion channel.

Chapter 3

Cross-Linked Carbon Nanotube Fiber

3.1 Introduction

Carbon nanotube (CNT) [3] is believed to have many practical applications in the coming era of nano technology because of the mechanical [4, 62] and electronic properties [63, 64, 65, 66]. Although a major portion of current studies are focused on production and properties of the ideal tubes, their structural variants, *e.g.* Y-shaped tubes [67], tube junctions [68, 69, 70], and functionalized nanotubes with other atoms [71] or small cluster [72] have drawn increasing attention. All these CNT-derived systems are expected to be closer to practical applications than the ideal tubes, including the carbon nanotube fiber.

Since the discovery of CNT, individual CNT has been demonstrated to possess a ultrahigh Young's modulus and tensile strength by theoretical prediction TPa [4, 73, 74] first and experimental confirmation [62, 75], recently. However, due to the weak van der Waals [76] interaction between side walls of nanotubes the reported values for the strength of SWNT bundles are much less than the individual nanotube, which is only up to 100 GPa [77, 78, 79]. Intuitively, chemical bonds and functionals have

been introduced successfully to reinforce materials by both theoriticians [80, 81] and experimentalists [82, 83, 84] as cross links between CNT or between CNT and polymer matrix.

3.2 Carbon Links

Before considering other chemical species, our investigation begins with carbon links between the single walled CNT's by energetics calculation using a density functional tight-binding force model [7, 12, 13] and molecular dynamics (MD) simulation. Periodic boundary condition is applied in the axis direction of the tubes, with the computational super-cell chosen long enough to eliminate the interaction between the links. Two extreme chiralities, *i.e.* the armchair tubes with index of (n, n) and the zigzag tubes with index of (n, 0), were considered. Formation energies of those links between parallel identical CNT's were calculated with respect to diameter and chirality to extract basic energetics conditions that stabilize the links.

The formation energy of a C_{2n} link is defined as:

$$\epsilon_f = \left[E^{tot} - \left(2 \times E^{tot}_{tube} + n \times E^{tot}_{dimer} \right) \right] / n, \tag{3.1}$$

where E^{tot}, E^{tot}_{tube} and E^{tot}_{dimer} are total energy of the linked system, the ideal tube and the isolated carbon dimer, respectively. Such formation energy measure is closely related to the strength of the link.
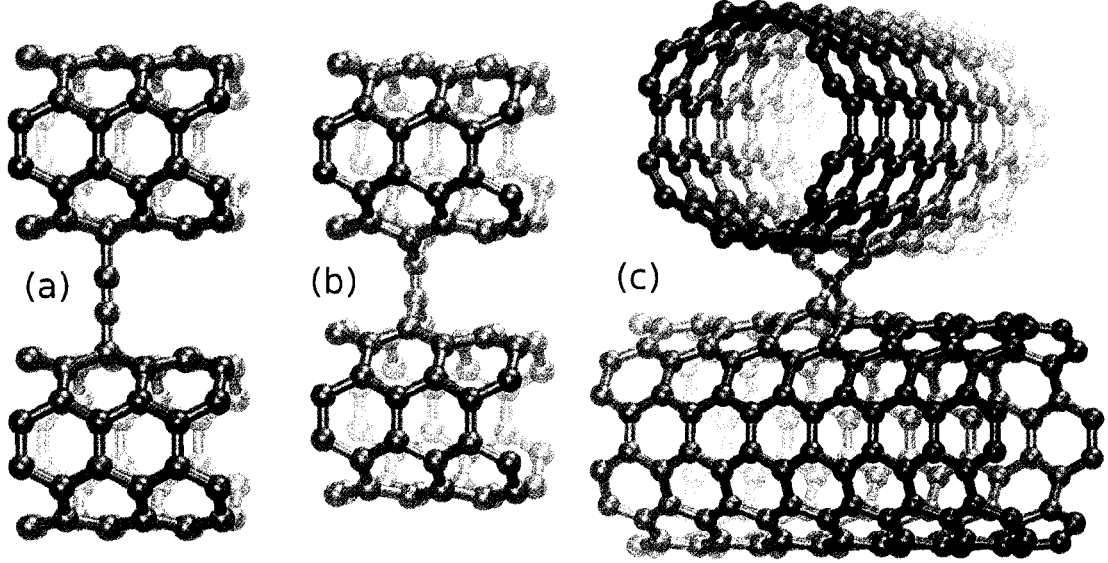
Figure 3.1 (a) Top-site and (b) bridge-site C_2 links between two parallel (4, 4) nanotubes; (c) >C< cross-link is formed between two (6, 6) nanotubes.

3.2.1 Length of Cross Link

Due to van der Waals interaction between carbon nanotubes, the equilibrium distance between side walls of two parallel CNT is 3.5 $\mathring{A}$ [76]. This spacing is approximately enough for a link consisting of no more than two carbon atoms to fit in, because this spacing is roughly three times that of a C$-$C bond length.

Therefore, we insert a C_2 molecule between two parallel nanotubes. By running MD simulations around $1,000$ K, we search for different possible stable cross-linked structures. Two typical linked structures are found: Top-site (linear) and bridge-site (planar). In Fig. 3.1, we show the ball-and-stick models of these two links.

The chemical bonds in the top-site link is quite similar to those in the Acetylene

(H$-$C$\equiv$C$-$H), but each hydrogen atom is replaced by one nanotube. This link itself has a strong triple bond, while the bonding between the link carbon and the carbon on the nanotube side wall is a much weaker single bond. This bonding causes the rehybridization of this carbon on the nanotube side-wall, from sp^2 (graphite like) to sp^3 (diamond like) in assistance of the curvature effect, which helps the pyramidization [85]. However, the thicker the nanotube diameter is, the less significant the sp^3 rehybridization becomes. In addition, the equilibrium spacing between tubes for the top-site is around 4.0 $\mathring{A}$, which is greater than the spacing in bridge-site, 3.6 $\mathring{A}$. Therefore, the top-site link is less favorable, compared to the bridge-site link, *e.g.* the formation energy of top-site link is 2.5 *eV* weaker than the bridge-site link between two (4, 4) tubes, even without considering the energy cost to push tubes away from the van der Waals equilibrium distance. Therefore, we will focus on only the bridge-site links hereafter.

For the bridge-site C_2 link, each end of the link splits a C$-$C bond on one tube but form two new bridge bonds at the same time, so that sp^2 hybridization remains on the tube. The bond between the two carbon in the link is a double bond but is sp^2 in nature as well. Consequently, the link splitting the most curved bond (the weakest) is the most favorable, and releases the most strain energy. For example, the formation energy of a bridge-link splitting the horizontal bonds (parallel to the axis) on the zigzag (7,0) tubes is 4.5 *eV* stronger than that of the link splitting the vertical

bonds (perpendicular to the axis) on the arm-chair (4,4) tubes. The more strain that is released, the stronger the link that is formed.

Notably, we obtain an interesting bridge-site link with single carbon atom sitting between two tubes. The only carbon atom of the link breaks one bond on each tube, and forms four bonds with four different carbon atoms on the tubes. Such a link formed between two (6, 6) tubes is shown in Fig. 3.1 (c). This type of link appears stable, but the van der Waals repulsion makes this kind of link impractical unless very high pressure is present.

3.2.2 $-C_{2n}-$ Cross Link

The formation energy of a cross link is strongly dependent on the strain energy of the bonds being split by the cross link. Since the strain energy originates from the curvature of the rolled graphene sheet, the formation energy of the link is diameter dependent. The diameter-dependence of the formation energy is shown in Fig. 3.2. For each chirality, three non-equivalent cross links can form, because there are three different bonds on each nanotube. However, for the armchair and zigzag tubes, there are only two possible links due to the tube symmetry. In Fig. 3.2, we only show the links with lower formation energies. In other words, we choose to show the most stable ones for each case, $i.e.$, for armchair (zigzag) tubes we choose the one splitting the vertical (chiral) bonds. From the figure, one can see that in both cases the formation

energy becomes weaker as the diameter increases. The cross links formed between armchair tubes are stronger than those formed between zigzag tubes with a similar diameter, although the difference tends to decrease, and eventually converges to zero when the diameter approaches infinity, which is the graphene sheet.

Since C_2 addimer is one of the most well-known isomers [55, 56], it is interesting to compare the formation energy of the links with the on-wall addimers. The on-wall addimer also splits two C−C bonds but in the same hexagon on the same nanotube. As well as the bridge-site links, the addimer parallel to the axis of the armchair tube [Fig. 3.3 (a)] is the most stable one among all different addimers. On a zigzag tube, the addimer splitting the chiral bonds [Fig. 3.3 (a)] is found to be $0.4 \sim 0.8$ eV stronger than the horizontal addimer [Fig. 3.2] within the diameter range of $4 \sim 10$ Å. Therefore, the formation energies of the chiral addimers on (n, 0) and the horizontal addimer on (n,n) tubes are calculated against the diameter and shown in Fig. 3.2. From the figure, one can see that the addimers are more stable than the C_2 links when the tube diameter is greater than 6 Å. Therefore, smaller diameter is more favorable for the formation of C_2 links.

In the optimized addimer structures, two interstitial carbon atoms pop out of the nanotube side-wall significantly. This indicates the existence of the mixture of sp^3 and sp^2 hybridizations, and implies the dangling bond on top of the adatoms making the addimer radical. When we bring two tubes closer than van der Waals spacing
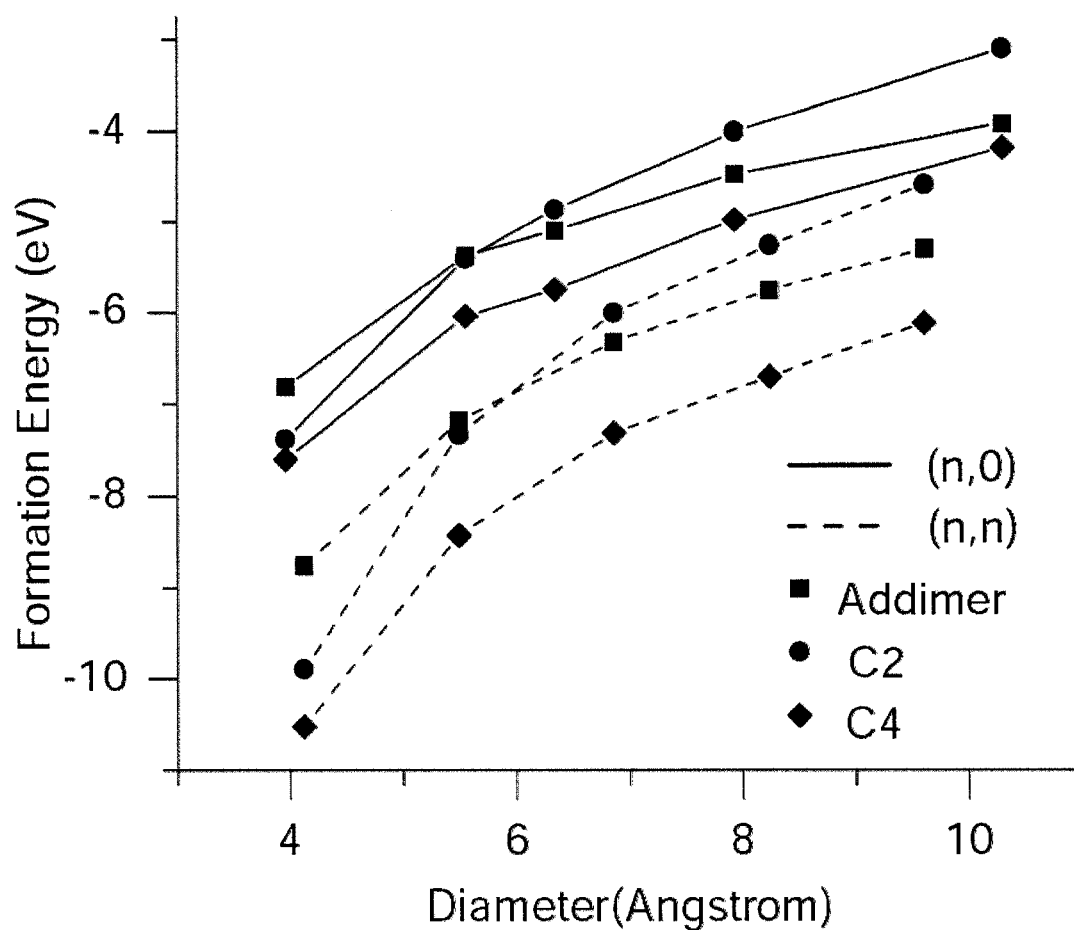
Figure 3.2 Diameter-dependent formation energy of on-wall addimer and C_2, C_4 links between parallel tubes. The C_2 links are bridge-site links splitting chiral and vertical bonds, respectively, in the zig-zag and armchair tubes. C_4 links are made of addimers face-to-face.
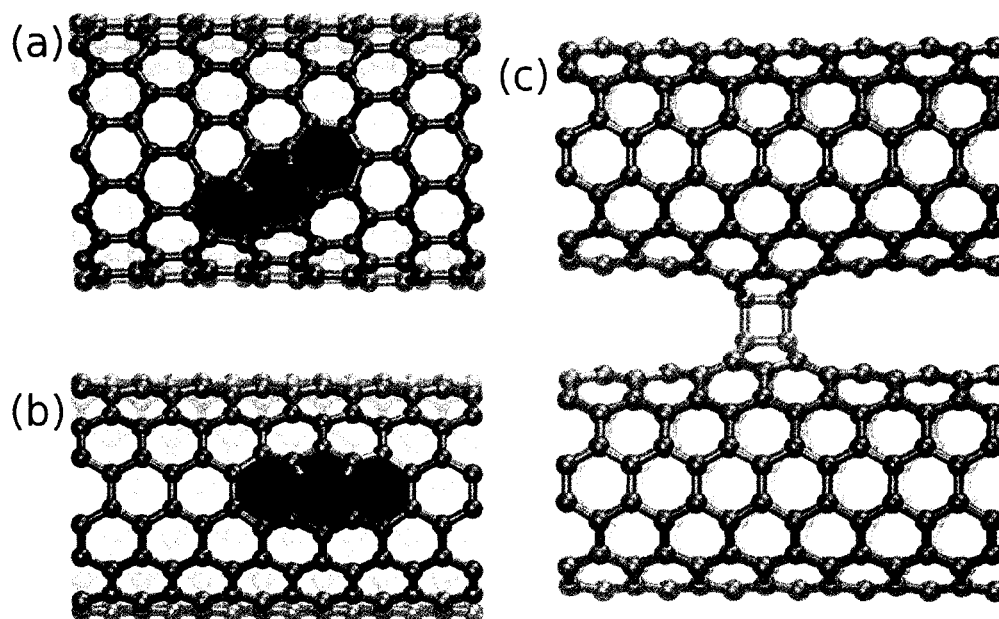
Figure 3.3 (a) Chiral addimer on a zig-zag tube: a C_2 molecule (red atoms) splits two facing chiral bonds and a $7/5/5/7$ defects is formed. (b) Horizontal addimer on an armchair tube: two vertical bonds are split. (c) C_4 cross link formed by two addimers on arm-chair tubes, which are C_2 molecules parallel to the axis splitting the vertical bonds on (6, 6) nanotubes.

with one addimer right above the other, the dangling bonds are saturated by forming a C_4 link. Therefore, we also include the diameter-dependent formation energy of the C_4 links in Fig. 3.2 as well as the C_2 links and addimers. For all the tube diameters we investigate, the formation energy of C_4 link is always lower than that of the addimer on the same tube.

Furthermore, we extend this C_4 link to C_{2n} with $n = 1, 2, \ldots, 6$, where n is corresponding to the number of bonds split in one hexagon on each tube. Although there are more than one nonequivalent structures for each n except for $n = 6$, one can always figure out easily the most stable configuration by determining the weakness of the bonds being split. The formation energies for the links ($n =4$, 5, and 6) between (6, 6) tubes are shown in Fig. 3.4, and it turns out that the C_8 link is the most stable.
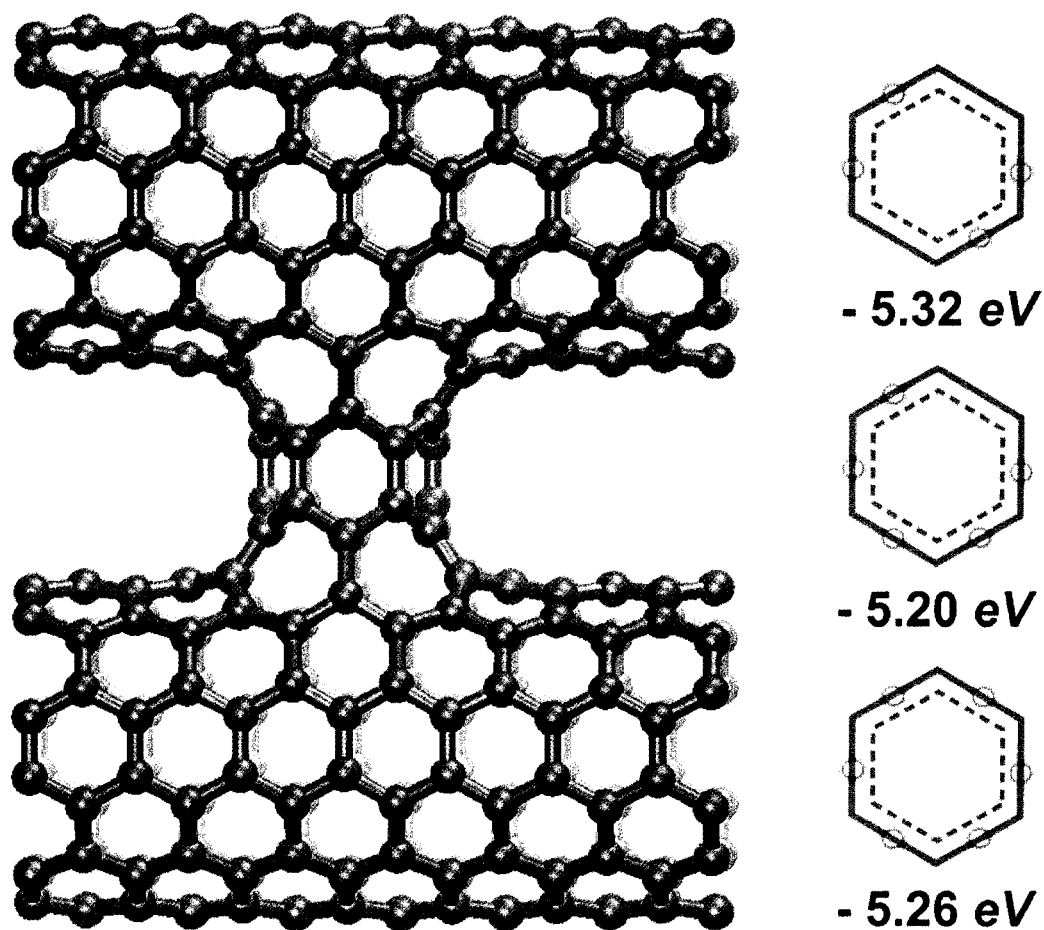
Figure 3.4 C_{2n} links between two (6, 6) tubes for $n = 4, 5, 6$. (a) Ball-and-stick illustration for $n = 6$; (b) Schematic diagram for $n = 4, 5, 6$. Open circles denote sites occupied by a C_2 link.

3.3   Relocation of Cross Link on Nanotube: MD Simulation

In the last section, we have investigated different C_{2n} links. We will study the shear strength of the interface between two individual nanotubes, which essentially determines the strength of the CNT fiber in this section. For simplicity and for the sake of revealing the physics of the mechanism, we take a simple C_2 link as an example throughout this chapter. Due to the lack of the experimental evidence, we perform MD simulations to understand the mechanism of the failure in the cross-linked nanotube fibers. Finally, we connect it to the macroscopic strength of the fiber.

In our MD simulations, two nanotubes are aligned parallel to each other in the manner that tubes align in the bundle. For computational convenience, we truncate the nanotubes to a finite length from 1.2 nm up to 2.4 nm in different simulations. Therefore, we employ hydrogen atoms to terminate all ends of the tubes by saturating the dangling bonds. In order to reveal the essential physical phenomenon, all calculations in this section are conducted with one consistent semi-empirical method, AM1 [17]. It is relatively more accurate than the classical potential methods [2] and even the tight-binding (TB) method [7] (TB is usually not good for describing the chemical reactions), but much computationally cheaper than any density functional theory (DFT) methods [21]. Two software packages, Gaussian-03 [19] and Dynamo [20], are employed to perform the geometry optimization, the transition

state searching and the molecular dynamics (MD) simulation. Shear strain is applied horizontally on one end of each tube in the opposite direction. In order to represent the van der Waals interaction between side walls, all the ends are constrained to move only in parallel to the axis of the nanotubes. Although the studies on how the normal force applied on the nanotubes' interface influence the resistant force against the shear is also important and interesting, we don't include them in this chapter. The shear displacement is prescribed by the shear rate and the time step of the MD simulation.

After shear strain is applied, the nanotubes slide away from each other. The link connecting the tubes is deformed/stretched, and the strain energy is accumulated. Depending on the simulation temperature, the cross-link is eventually broken at different shear displacements. Between two carbon atoms of the link itself are sharing a double bond which is similar to the bonding between the carbon atoms in ethylene. This double bond is much stronger than the single bond between carbon of the link and carbon on the side walls of the nanotubes. Consequently, the link only breaks at the connecting points on the side walls. After the link is broken, the system stays in very high energy state, due to the dangling bonds created thereafter. Interestingly, the dangling link slips forward and reconnects with other carbon atoms on the tubes. This phenomenon of link relocation not only enhances the modulus and strength of the nanotube fibers but also keeps the cross-link intact.
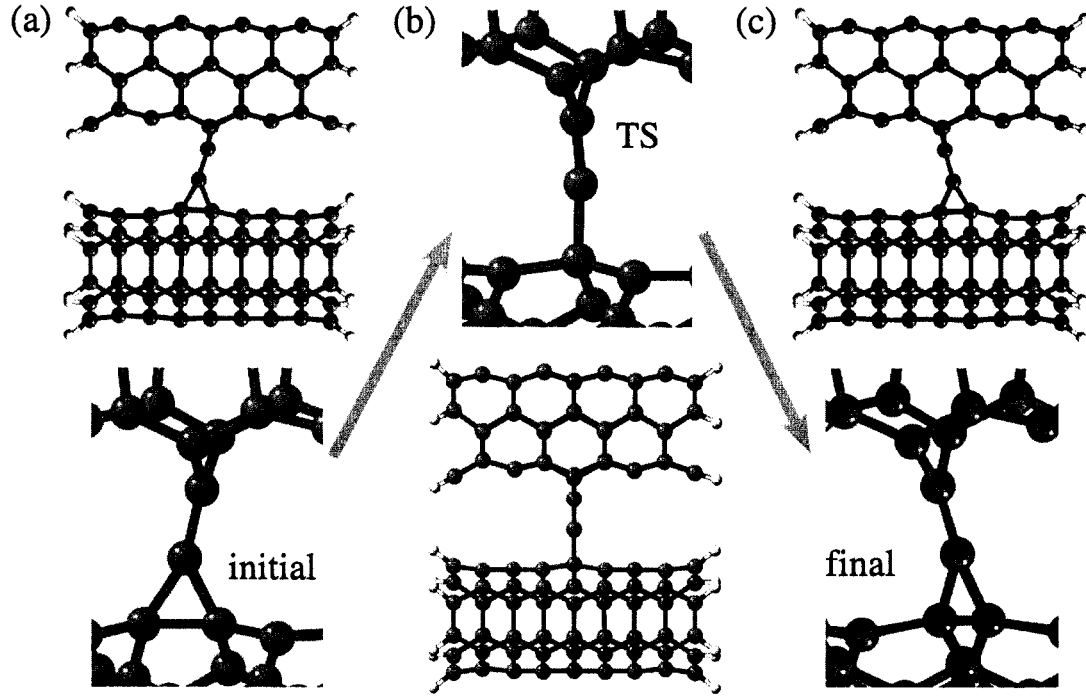
Figure 3.5   Two (3,3) SWNT with a >C=C< cross-link: (a) initial state; (b) transition state; (c) final state.

As an example, we pick two (3, 3) SWNT are cross linked by $-C = C-$, shown in Fig. 3.5. This cross-link forms two bonds (legs) with each nanotube. In order to simplify the problem, we intentionally choose the contact between link and one (upper) tube stronger than the contact on the other (lower) tube. The two upper "legs" are formed between the link and two carbon atoms associated with an armchair bond at the bottom of the upper tube; and the two lower "legs" are formed between the link and two carbon atoms associated with the chiral bond in the zigzag path on the top of the lower tube.

One of two bonds connecting with the lower SWNT is stretched more than others.

With the help of thermal vibration, this most stretched "leg" will break eventually after a long enough duration time. Then, the link slides forward along the tube axis, and forms a new "leg" with the next available side-walled carbon along the zigzag path. This relocation of the cross-link is repeatable, since the cross-link is healed by itself. However, each relocation event can be considered as "creep" failure, and is influenced by the simulation temperature and the shear rate. The higher the temperature or the more slowly the SWNT are sheared, the further the cross-link can be dragged along the axis. In a simulation with the temperature of 300 K and the shear rate of 0.1 nm/ps, we observed the relocation occurring when the shear displacement is 2.27 $\mathring{A}$.

3.4 Phenomenological Model

Upon our observations in MD "experiments", we proposed a phenomenological model to investigate the friction/resistant force, which determines the strength of the bundle essentially. In our model, the interface consists of two parallel surfaces connected by the cross-links, which is illustrated in Fig. 3.6 (a). The upper surface is pulled horizontally away from the fixed lower surface. For simplicity, the lower contact between the links and the surfaces is assumed to be weaker than the upper one, so the links are only allowed to relocate on the lower surface. Since the chemical bonding can not be formed at an arbitrary position on an atomic surface, the lower
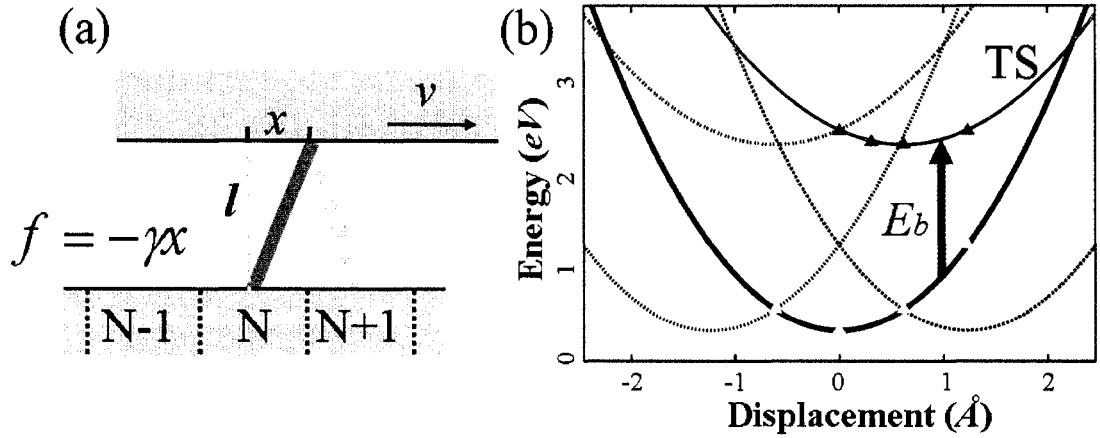
Figure 3.6 (a) Sketch of the cross-linked model surfaces; (b) the potential energy and transition state energy landscapes of the cross-linked system in function of displacement.

surface is divided into sites, which represent the periodicity. Each link must attach at the center of one site at any moment. The spacing between two surfaces is fixed to the intact length of a link, h.

When the upper surface is pulled away from site **N**, the shear strain is accumulated around the links, because of the creep deformation. Although the energy surface in terms of the shear displacement x can be numerically computed, the elastic link approximately behaves like a rubber band, and the potential energy of one link increases parabolically as it is stretched: $E_N(x) = E_0 + \frac{1}{2}\gamma(x - Na)^2$, where E_0 is the potential energy of a intact link and γ is the force constant. The potential surface according to the shear displacement is plotted in Fig. 3.6 (b) as a (black) parabola, while the two dashed parabolas represent the energy surfaces when the cross link is formed at site **N+1** (green) and site **N-1** (blue), respectively. Due

to the periodicity, all individual energy surfaces associated with different sites have one identical shape, but shifted from the nearest neighbor by a periodicity a. They overlap with each other and form a hyper-energy-surface, which has multiple values for a given displacement, because a cross-link can connect with different sites at one position. Furthermore, the energy barrier preventing cross-links from moving from one site to the other is a multiple value function of the shear displacement as well, and the landscape of it can also be treated as a (red) parabola shown in Fig. 3.6 (b): $E_{ts_{N \leftrightarrow N+1}}(x) = \varepsilon_{ts} + \frac{1}{2}\gamma_{ts}\left(x - \frac{2N+1}{2}a\right)^2$. The local extrema of the transition state energy is due to the symmetry that the process to move a link forward from site **N** to site **N+1** at $(a/2 - x')$ is identical to the process of moving that link backward from site **N+1** to site **N** at $(a/2 + x')$.

According to the transition state theory (TST) [86] and our previous works [87], the transition probabilities for a link to relocate from site **N** to site **N+1** in unit time interval can be expressed as follows,

$$dt \cdot K_{N \rightarrow N+1} = dx \cdot \frac{\nu}{v} \exp\left[-\frac{E_{b_{N \rightarrow N+1}}(x)}{k_B T}\right], \tag{3.2}$$

in which, the attempt frequency [86, 87] $\nu = k_B T/2\pi\hbar$, $E_{b_{N \rightarrow N+1}} = E_{ts_{N \leftrightarrow N+1}} - E_N$, v is the shear rate and k_B is the Boltzmann's constant. Therefore, the slower the link is pulled or the higher the temperature is, the higher probability for a link to relocate. During the creep failure, the potential energy lost is mainly converted into

the incoherent kinetic energy, which is the heat produced by the macroscopic friction. By tracking either the instantaneous friction force or the energy lost during creeping, we can calculate the dynamical friction after all the parameters introduced in our model are computed.

Table 3.1 Parameters of two (3,3) nanotubes with a C_2 cross-link, determined by AM1 [17] method.

$a(\mathring{A})$	$\gamma(eV/\mathring{A}^2)$	$\varepsilon_{ts} - E_0(eV)$	$\gamma_{ts}(eV/\mathring{A}^2)$
1.23	1.224	2.014	0.816

3.5   Shear Rate and Temperature Dependent Strength

For a single link, the creep process described above is a time-dependent infinite cascade levels problem as follows:

$$\dot{\rho}_i(t) = \sum_j K_{j \to i}(t)\rho_j(t) - K_{j \leftarrow i}(t)\rho_i(t) \tag{3.3}$$

in which, $\rho_i(t)$ is the probability for a link to connect with the ith site at time t, and the initial condition is as follows: $\rho_N(0) = 1$ and $\rho_{i \neq N}(0) = 0$. Since there is no way to obtain a general solution for it, we begin with the extreme cases: i. high shear rate or low temperature; ii. low shear rate or high temperature.

3.5.1 High Shear Rate or Low Temperature Limit

For the first case: $a \cdot \nu \exp\left[-E_b(-\frac{a}{2})/k_B T\right] \ll v$, the shear rate is so high (or the temperature is so low) that the probability for a link to move backward is nearly zero during the whole shear process. The movement of the links becomes stick-slip motion [88]: stick for one period and slip at the average "creep" failure position, $\bar{x}$, where the transition probability integral reaches unity: $\int_{\bar{x}-a}^{\bar{x}} dt \cdot K_{\rightarrow} = 1$. Substitution of Eq. (3.2) into the integral yields the solution:

$$\frac{1}{2}\left(\gamma - \gamma_{ts}\right)\left(\bar{x} + x_0\right)^2 - \Delta E = k_B T \ln\left[\frac{2\pi\hbar v\left(\gamma - \gamma_{ts}\right)\left(\bar{x} + x_0\right)}{k_B^2 T^2}\right] \tag{3.4}$$

in which, $x_0 = \frac{\gamma_{ts}}{\gamma - \gamma_{ts}}\frac{a}{2}$, and the maximum energy barrier $\Delta E = \varepsilon_{ts} - E_0 + \frac{\gamma\gamma_{ts}}{\gamma - \gamma_{ts}}\frac{a^2}{8}$. Notably, although the solution shown here is for $\gamma > \gamma_{ts}$, the results for those cases, which have solutions for $E_b(x) = 0$, are similar to it. For the case, whose crossing point between energy surface and transition energy surface is less than $\frac{a}{2}$, the motion of the system is better described as breaking and reforming the cross-link [89], although the recipe to study the friction is still applicable only through changing the model reaction.

Because the energy lost equals the work done in one period, $f = \left[E(\bar{x}) - E'(\bar{x})\right]/a = \gamma\left(x - \frac{a}{2}\right)$. The critical strength is linearly proportional to the mean failure position, $\bar{x}$, so the strength of the bundle increases monotonically as the shear rate rises. However, the friction cannot increase arbitrarily because the link will relocate immediately

when the energy barrier becomes zero:

$$\frac{1}{2}\left(\gamma - \gamma_{ts}\right)\left(\bar{x}_{max} + x_0\right)^2 - \Delta E = 0 \tag{3.5}$$

Therefore, a rate-dependent friction [90] can be shown as follows:

$$f(v) \approx f_{max}\left[1 + \beta \ln\left(\frac{v}{v_c}\right)\right] \tag{3.6}$$

in which, the coefficient $\beta = \frac{k_B T}{\Delta E} \cdot \frac{\sqrt{2\Delta E(\gamma - \gamma_{ts})}}{2\sqrt{2\Delta E(\gamma - \gamma_{ts})} - \gamma a}$. When the shear rate reaches the critical value: $v_c = \frac{k_B^2 T^2}{2\pi\hbar(\gamma - \gamma_{ts})(\bar{x}_{max} + x_0)}$, the average dynamical friction is maximized, $f_{max} = \gamma\left[\sqrt{\frac{2\Delta E}{\gamma - \gamma_{ts}}} - \frac{\gamma}{\gamma - \gamma_{ts}}\frac{a}{2}\right]$. Likewise, the temperature dependent friction law can also be shown as, $f(T) \approx f_{max}\left[1 - \frac{T}{\Theta}\ln\left(\frac{T}{T_c}\right)\right]$, in which, $\Theta = T/\beta$, and $T_c = \sqrt{2\pi\hbar v\left(\gamma - \gamma_{ts}\right)\left(\bar{x}_{max} + x_0\right)}/k_B$.

3.5.2 Low Shear Rate or High Temperature Limit

The second case is: $0 < v \ll a \cdot \nu \exp\left[-E_b(0)/k_B T\right]$, in which the shear rate is low enough or the reaction barrier is relatively low compared to the temperature. The cross-links can easily overcome the energy barrier, so the "occupants" for the cross-link connecting with different sites are able to reach thermal equilibrium after a delay. Since the cross-links can relocate anywhere during the shear process, we need to integrate all the energy lost in one period in order to calculate the average dynamical friction:

$$f = \frac{\int dW}{a} = C\frac{2\pi\hbar\gamma v}{k_B T}e^{\frac{\varepsilon_{ts} - E_0 - \frac{a^2}{k}}{k_B T}} \tag{3.7}$$

in which, C is a pre-factor. Therefore, the friction in this limit is fluid-liked, which is linearly depending on the shear rate. The viscosity can be defined as: $\mu = C\frac{2\pi\hbar\gamma A}{k_B Th}e^{\frac{\epsilon_{ts}-E_0-\frac{a^2}{8}}{k_B T}}$, in which, A is the effect contact area for one link, and h is spacing between two surfaces. Clearly, the viscosity increases when the temperature drops dramatically. And, the contact area A is directly related to the density of the cross-link. The higher density of the cross-link, the greater is the viscosity. The force constant in the nominator means that the stronger the cross-links are, the thicker this "fluid" is.

3.6 MC Simulation

Now, we go back to the two (3,3) SWNT and >C=C< link, whose parameters are tabulated in Tab. 3.1. Although for this particular link all the realistic shear rates and temperatures are in the high shear rate or low temperature regime, we employ Monte Carlo (MC) [31] simulation in order to provide a method for general study and to confirm our analytical solutions.

In our MC simulations, there are L SWNT interfaces, and in each interface there are M cross-links. The displacements of the links belonging to the same interface are in phase, which means they can only differ by integer times of the periodicity. All the interfaces are sheared simultaneously by a sufficiently small distance. For each movement, the probabilities for a single cross-link to slide forward or backward are

computed and compared with a random number generated, and then the cross-links will stay or move to the neighboring sites, accordingly. The dynamical friction of 1000 cross links between two (3,3) nanotubes at 300 K is shown in Fig. 3.7 (a) with a shear rate, $v = 4.0 \times 10^{-7} \mathring{A}/ns$ [91]. The friction linearly increases as an elastic force, and suddenly drops when it reaches the maximum static friction force (f_{static}) about $3.3 nN$. Accordingly, the potential energy is lost periodically around the average creep failure point,$\cdot \bar{x}$, shown in Fig. 3.7 (b). By averaging the instantaneous resistant force, we can get the average dynamic friction for corresponding shear rate and temperature. Fig. 3.7 (c) shows that the average dynamical friction is logarithmically dependent on the shear rate with a fixed temperature, and confirms the shear rate and friction relationship as Eq. (3.6) shows.

In addition, one can calculate the shear strength of the cross-links between carbon nanotubes as follows: $\sigma_{shear} \approx n_L f_{static}$, in which n_L is the number of the links for each carbon atom on the contact area. For two (3,3) SWNT with >C=C< links, the shear strength, $\sigma_{shear} \approx n_L \cdot 60 \ GPa$. Usually, $n_L \sim 10^{-2}$, so the shear strength is on the order of 1 GPa. However, the tensile strength of a bundle is as follows: $\sigma_{tensile} \approx \frac{2 l_{tube}}{r_{tube}} \sigma_{shear}$, in which l_{tube} is the average length of the nanotubes, and r_{tube} is the average radius of the nanotubes in the bundle. Since the ratio of the length and the radius can be up to 10^3, the tensile strength can reach the order of 1 TPa.
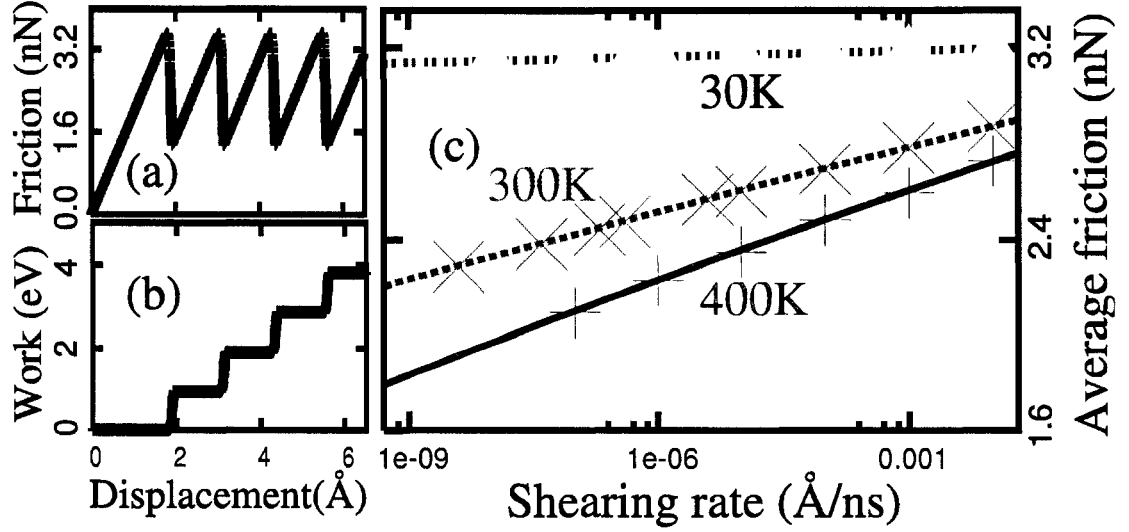
Figure 3.7 Monte Carlo simulations for the dynamical friction between two (3,3) SWNT with a C_2 cross-link: (a) instantaneous friction depending on the displacement, and (b) energy lost during the sliding with a shear rate, $4.0 \times 10^{-7} \mathring{A}/ns$ @ 300 K; (c) lines are theoretical values, points are the average dynamical friction simulated via MC method for different temperatures.

3.7 Other Links

Because of the existence of interstitial defects, it is straightforward for carbon to become one of the promising candidates for the cross-link. Among all the carbon links, -C=C- link is the best, because its length is close to the van der Waals spacing between nanotubes' side walls. However there are circumstances where we might need to examine the species other than carbon only.

The first example is the application of hydrogen storage. Carbon nanotube materials are expected to be one of the few best candidates for hydrogen storage due to the high surface-to-volume ratio and light, porous structure [92, 93]. However, raw

CNT materials often form bundles and the hydrogen storage in such tube bundles was found to be very low [94]. Theoretical analyses indicate that the short inter-tube separation distance within bundle prevents hydrogen molecules from accessing the space between the tubes [95, 96]. Based on this study, a further theoretical suggestion of increasing the van der Waals gap to about 0.7 nm was proposed as a solution to enhance the hydrogen storage in CNT fibers [93, 94, 95, 96]. Moreover, another theoretical consideration suggests that placing of parallel graphene layers every 0.7 nm could double the potential well depth for hydrogen absorption, and thus significantly enhance the hydrogen storage capacity at room temperature [93, 97].

One possible experimental route to achieve the well-separated single-walled carbon nanotube bundles is via chemical functionalization, which is the covalent attachment of functional groups to the adjacent tubes in the array bundle. At a certain concentration, such functional groups should be able to overcome the van der Waals attraction between tubes (typically around 1 eV/nm of length) and thus increase the tube-tube distance [98]. Based on this experiment, we propose to cross link the tubes with benzene. In Fig 3.8, we show the ball and stick models of two different cross-links: (a) p-phenylene and (b) biphenyl functionalized nanotube bundles [93]. After fully geometrical relaxation via density functional based tight-binding method [7, 13, 12], the former cross-link maintains a van der Waals gap at a nearly desirable value of 0.67 nm (wall to wall) with p-phenylene functional groups as the spacers between

tubes. Fig. 3.8 (c) shows three-dimensional material consisting of nanotubes and the p-phenylene cross-links. This cross-link plays two important roles: it makes the surface of the tubes accessible, and in addition the overlap of van der Waals potential nearly double the binding energy at the bottom of the well.

We also propose several other links with different species, including boron and oxygen. Both of these linked structures are optimized with the AM1 method, and are shown in Fig. 3.9.

3.8 Conclusion

In summary, $>$C$=$C$<$ cross-link is one of the most stable cross-links formed between two parallel SWNT. The finite temperature AM1 MD "experiments" on two (3, 3) nanotubes revealed the creep of this cross-link in the nanotube bundles or fibres, and suggested that creep of the cross-links can be the origin of the dynamical friction and the strength of the bundle. We proposed a phenomenological model, whose parameters can all be determined by quantum chemistry methods. Analytical solutions of the dynamical friction were shown for two limits: i. the logarithmic dependency of the stick-slip friction on the shear rate or temperature was shown for high shear rate or low temperature; ii. fluid liked friction linearly depending on the shear rate was shown for the low shear rate. Monte Carlo simulations were further employed to study the friction under general conditions. We show the shear strength of a bundle
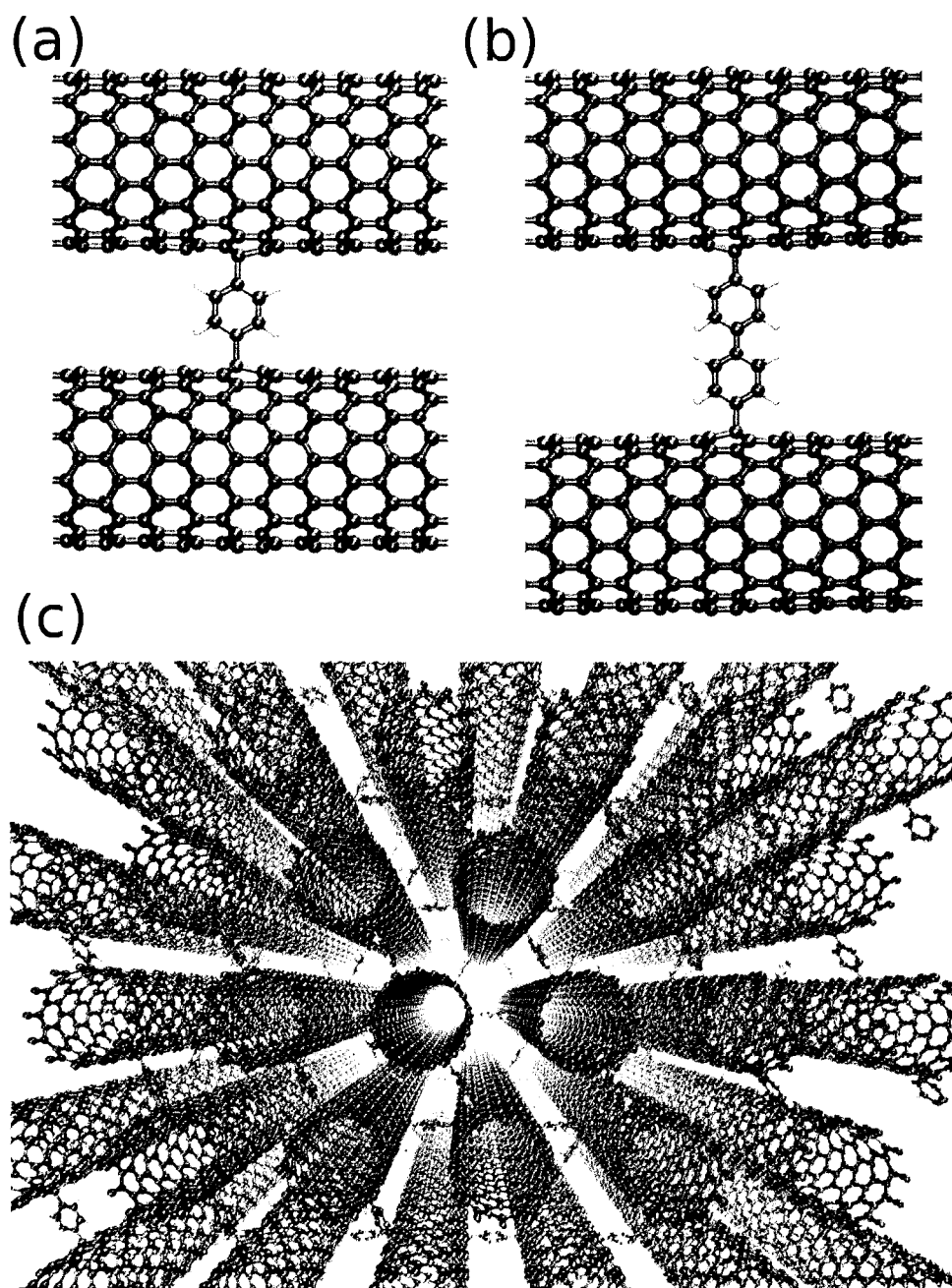
Figure 3.8 (a) *p*-phenylene, (b) biphenyl cross-links; (c) nanotube bundles with *p*-phenylene functional cross-links.
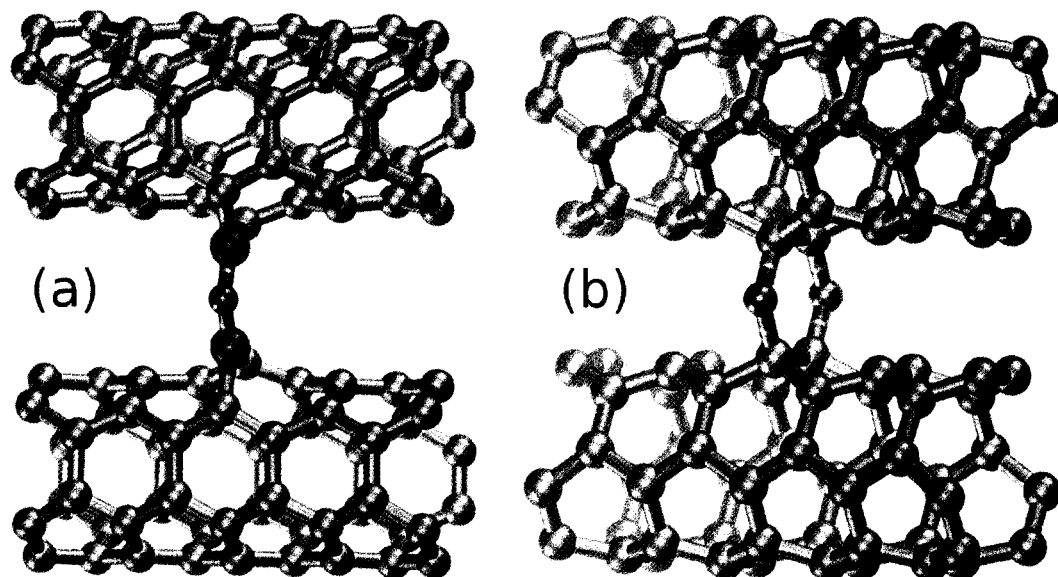
Figure 3.9 (a) -B-O-B- link; (b) O_2 link

with the cross-link is less than 100 GPa, but the tensile strength can be up to 1 TPa.

Chapter 4

Pentagonal Silicon Nanowire

4.1 Introduction

Highly anisotropic silicon nanowire (SiNW) is drawing ever growing attention from both theoretical and experimental workers. This is because the continuous advances of computer engineering technologies are driving the size of silicon-based electronic devices towards their limits. Quantum mechanics confinement effects become dominant in this case. Moreover, silicon nanowires' relative simplicity and compatibility with traditional techniques make it one of the promising building blocks for the next generation of electronic circuits. These potential applications in nano-electronics [99, 100, 101, 102, 103, 104] greatly stimulate this research interest in SiNW.

In this chapter, we start with generalized Wulff's theory for the quasi-one dimensional materials, and propose a family of stress-free ultra-thin silicon nanowires. After we conclude the ground-state structure of pristine SiNW [103, 105], we further study the electronic structures of the ground-state SiNW, and the relationship between the conductivity and the surface dimerization. In the last part of the chapter,

we demonstrate the hydrogen-passivated nanowires [106, 107, 108, 109, 110].

4.2 Pentagonal Silicon Nanowire

As we addressed previously, silicon has exclusive compatibility with the traditional electronic industrial techniques. Additionally, silicon has relatively higher chemical reactivity than other materials which facilitate doping [111]. Recent research reports indicate ultra-thin SiNW possessing novel properties, *e.g.* electronic and optical, which could be utilized in future applications. However, some of the basic issues remain unsettled, including the ground-state structure of the nanowire.

4.2.1 Generalized Wulff's Construction

In material science, Wulff has given a solution [112] for more than fifty years to determine the shape of a small crystal, assuming the surface free energy reaches the minimum for a given volume (number of the atoms $N = const$). In other words, the surface energy, $\Gamma = \int \gamma(\vec{n})ds$, where γ is the surface energy at a given direction specified by a vector $\vec{n}$ normal to this surface.

$\gamma(\vec{n})$ is a continuous function, but according to the atomistic level understanding this function has cusp points everywhere. Because the surface energies usually will increase dramatically at the minimum of this surface energy function. For example, (100) has a local minimum surface energy, but even an infinitesimal disorientation,
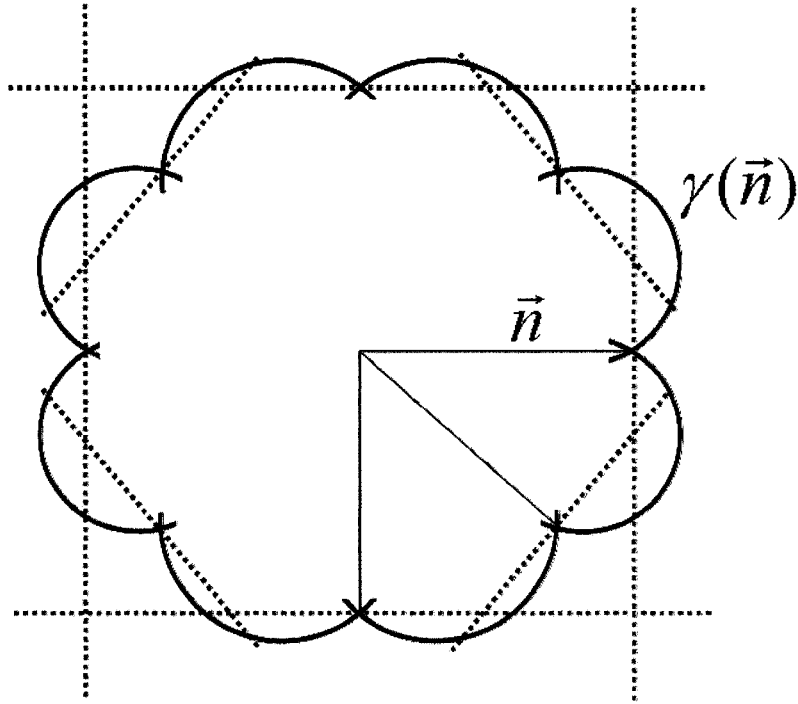
Figure 4.1 Wulff's reconstruction polar plot to determine the ground shape of a macroscopic wire. Enclosed solid curve is the surface energy function, $\gamma(\vec{n})$, and the dashed lines are drawn through cusps and perpendicular to the corresponding $\vec{n}$. The inermost polygon enclosed by dashed lines is the ground shape for the cross-section of the macroscopic wire.

e.g. (10n), can make the facet energetically unfavorable. Fig. 4.1 shows a typical

polar plot of a surface energy function. Starting from the local minima, one can draw

planes for 3D materials (or lines for 2D materials and quasi-1D materials), which

are perpendicular to the direction vectors. All these planes or lines will enclose a

minimal volume crystal. This shape will be the thermal equilibrium shape, which is

the ground structure.

To determine the ground state of the bulk silicon wires with a given thickness, classical Wulff's construction indeed can provide us a powerful recipe [112]. More specifically, one can get the cross section of the wire's ground structure by minimizing $\sum s\gamma_s$ with a constrain of $N = const$, where N is the number of the atoms in a cross-section of diameter $d \sim N^{1/2}$.

However, as the diameter goes down to the sub-micron range, one might notice that surface energy is not the only term determining the shape of the cross section. As the diameter decreases, the edge energy of a wire E_e ($\sim d^0 \sim N^0$) becomes more and more important and comparable with the surface contribution ($\sim s \sim d \sim N^{1/2}$), while we assume the bulk ($\sim d^2 \sim N$) has been minimized and thus invariant. For a silicon nanowire, N can be only a few dozen. Therefore, we revisit the Wulff's energy and pick up the edge energy term E_e, which is neglected:

$$F = E_e + \sum s\gamma_s + E_b \tag{4.1}$$

Consequently, the cross-section of a silicon nanowire will not only be determined by the facets, but also by the junctions between adjacent facets. In other words, one should pay more attention on how to fuse all the facets together in order to get the most stable silicon nanowire.

4.2.2 Pentagonal Shape Cross-Section

Even for nano-sized wires, the contribution from the bulk part ($\sim N$) is still considerably larger than the contributions from both the surface ($\sim N^{1/2}$) and the edge ($\sim N^0$). There is no much room to vary the bulk energy, E_b. Therefore, to find a ground state of SiNW, one should cut the wire from silicon bulk. Several possible pristine SiNW structures have been reported [113]. Furthermore, according to the generalized Wulff's energy 4.1, all the facets of the ground structure of a silicon nanowire should have the lowest or near lowest surface energy. In another word, one should cut the silicon prism along certain direction in order to create low energy surface only, for example (100) and {111} planes. One intuitive way of cutting is shown in Fig. 4.2. This prism has one (100) and two {111} planes. Obviously, all the edges of this pristine prism are having dangling bonds, which raises the energy of the wire. The last question becomes whether we can eliminate all the dangling bonds?

Interestingly, one of the angles of the prism $\alpha = 2\tan^{-1}\left(1/\sqrt{2}\right)$, which is very close to $2\pi/5$, with a deviation $\delta = \alpha - 2\pi/5 \approx 0.025$. Therefore, by putting five such prisms together, one can construct SiNW with a pentagonal shaped cross-section. Since the mismatch between adjacent prisms is proportional to the thickness of the wire, d, the energy cost (E_f) for the stacking faults [114] and the bulk shear [115] can be even negligible compared to the contributions from other terms. As a result,
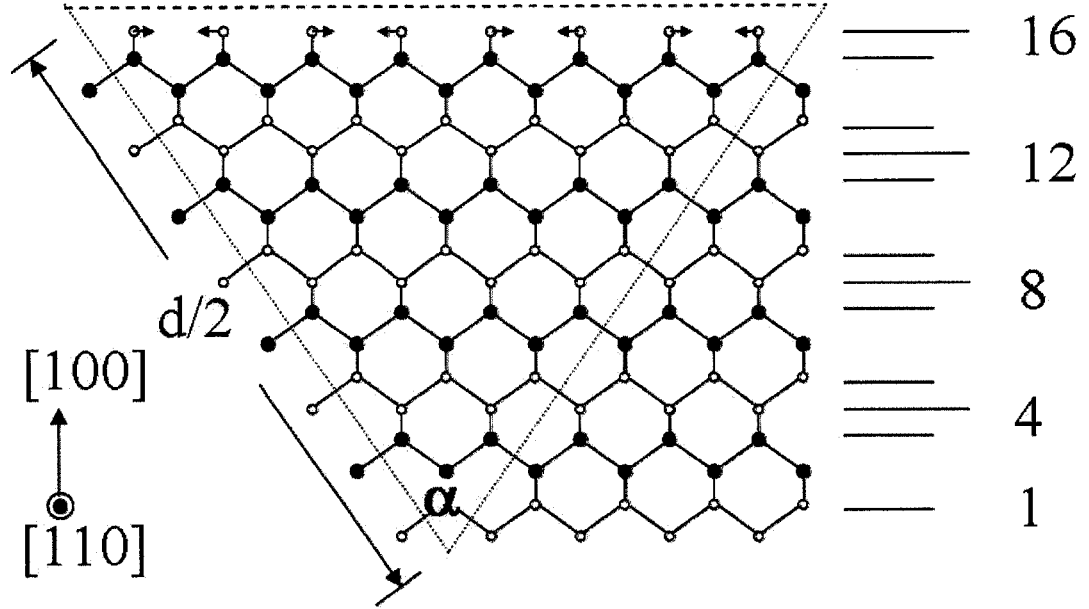
Figure 4.2 A prism cut from silicon crystal bulk.

all surfaces of this pentagonal quasi-crystal are (100) facets, which has relatively

low surface energy [116, 117]. However, the interface between adjacent facets is not

identical for all the pentagonal SiNW in this family. It can be divided into three

sub-families depending on the number of the layers in the prism: i) For those wires

having $4l$ atomic layers, there are even number of silicon atoms on each facet. All the

surface silicon atoms can pair up and form dimers, and the dimer rows are parallel

to the axis of the wire. We name this subfamily $P_{\parallel}$NW, shown in Fig. 4.3(a). ii) For

wires having $(4l - 2)$ layers, there are odd number of silicon atoms on the surface.

There are always dangling bonds remain unsaturated in this subfamily of SiNW, and

thus it will not be energetically favorable. iii) For those wires having $(2l - 1)$ atomic
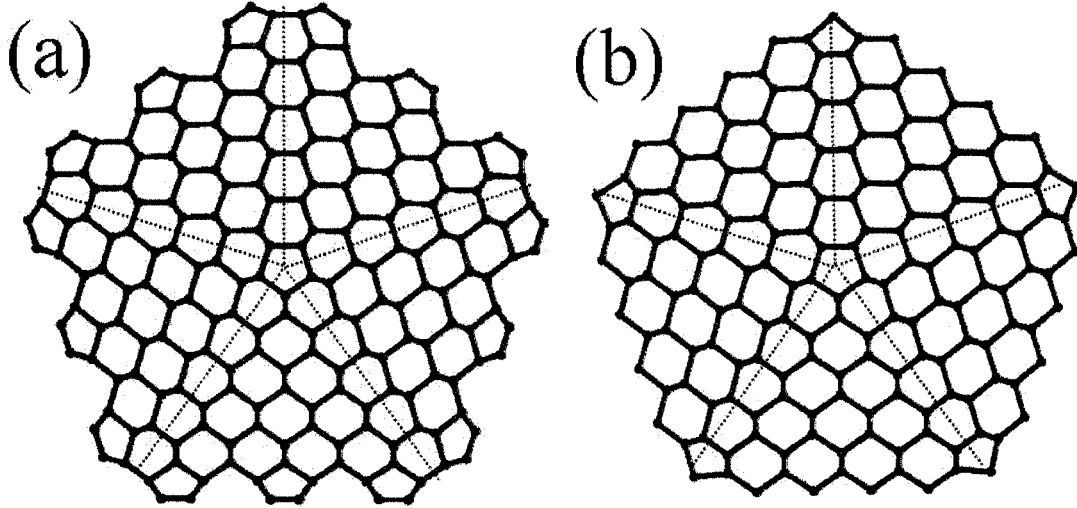
Figure 4.3 Two sub-families of the pentagonal silicon nanowires made of five silicon prisms: (a) $P_{\parallel}$, (b) $P_{\perp}$.

layers, surface atoms are not pairing up along the circumferential direction but the axial direction. Even or odd number of atoms does not effect the dimerization or surface reconstruction of these subfamily of SiNW. We name this subfamily $P_{\perp}$NW, shown in Fig. 4.3(b).

4.2.3 Ground State of the Thinnest SiNW

Now, we turn to examination of the stability of these pentagonal SiNW through energetic comparison among different SiNW, including hexagonal (H) and square (S) shapes. Usually, total energy will be chosen for such kind of comparison. However, one will notice that all the total energies are pretty close to each other, because the dominant contribution in the total energy is from bulk, E_b. For wires having the

same facets, the surface contribution does not vary either. The distraction from the bulk and surface energies makes the comparison rather impractical. Furthermore, the comparison here is among different SiNW families instead of several individual wires. In this case, direct calculation for all the wires is very expensive and calculation error may influence conclusion dramatically. Therefore, we decompose the total energy into different terms, and perform comparison of the excess surface energy,

$$S_0\Gamma = F - N\mathcal{E}_b - S_0\gamma_0 = E_e + \sum s\gamma_s - S_0\gamma_0 + E_f + \frac{1}{2}NK\epsilon^2 \qquad (4.2)$$

where, $\mathcal{E}_b$ is the unperturbed bulk energy, E_f is the stacking fault, $\frac{1}{2}NK\epsilon^2$ is the bulk shear, $\gamma_0 = 1.32 \ eV$ per a^2 area is the surface energy of Si(100) or Si{111} with (2×1) dimerization, and $S_0 = 2.11N^{1/2}$ is the effective surface area corresponds to the cylinder of diameter d, containing N atoms.

In order to demonstrate the validity and robustness of Eq. 4.2, we directly compute the excess surface energy with many-body empirical potentials (EP) [2], and density functional tight-binding force model (DFTB) [14] for some of the wires with smaller thickness. In Fig. 4.4, one can see the deduction of a large trivial contribution from $S_0\gamma_0$ reduces the error in absolute value of surface energy computed with different methods, and computed results corresponding to $P_\parallel$ and $P_\perp$ fit to a horizontal straight line (dashed, $\Gamma = 0$) and an inverse-linear curve (dotted, $\Gamma \sim 1/d$), respectively.

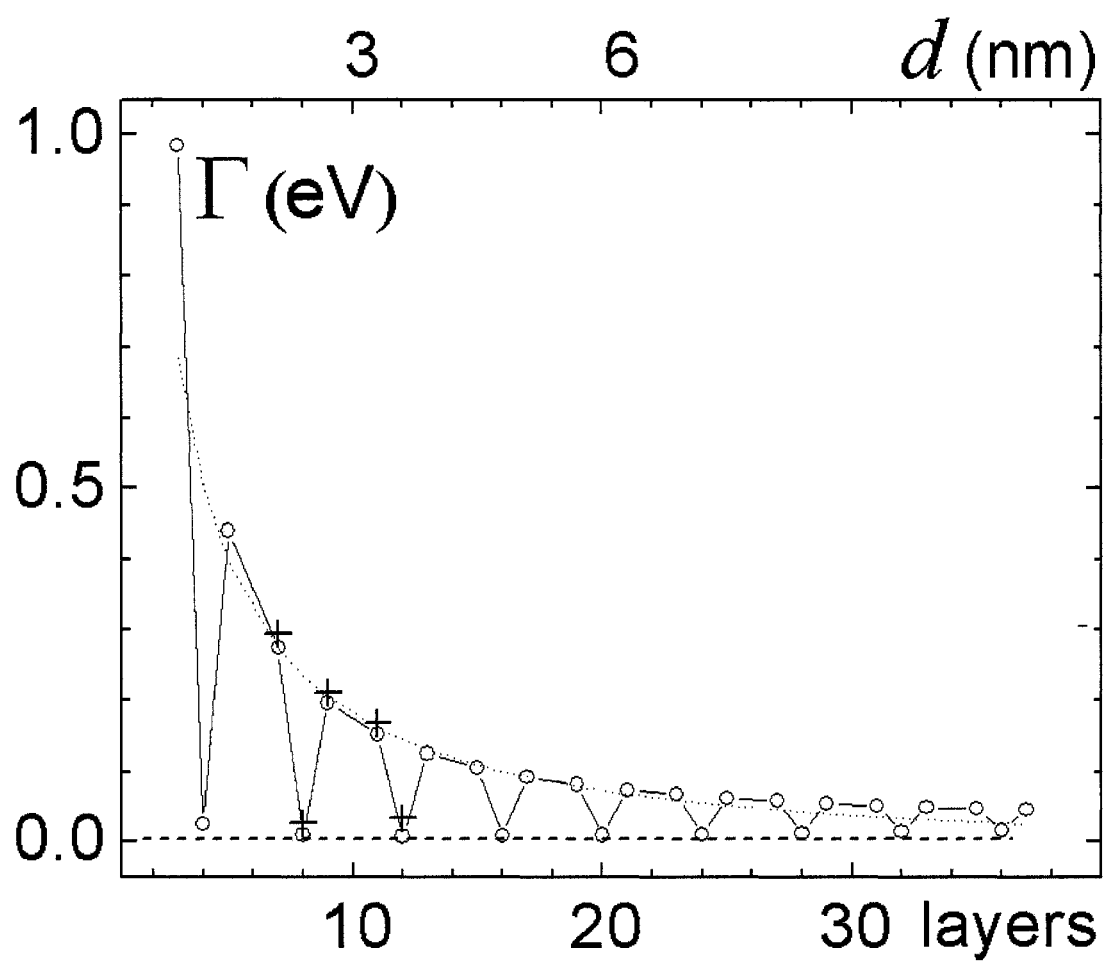Before we conduct the comparison, it is useful to corroborate the evidence of

Figure 4.4 Excess surface energy, computed with classical (circles) and TB (crosses), vs. the thickness of the pentagonal silicon nanowires.

Fig. 4.4 with an estimation. Energy modeling of complex surface based on simpler surfaces has been proved to be successful [114]. For example, in the square shape SiNW, each edge has a three-coordinated atom in a length of $\sqrt{2}a$. This edge atom cannot be counted as standard (100) surface atom. The surface energy of the relaxed {111} per surface atom is about $1.37eV$, therefore, $E_e = 4 \times \mathcal{E}_e = 4 \times 1.37/\sqrt{2} = 3.88\ eV$. In another word, the edge-energy can be estimated by the number of dangling bonds multiplied by the dangling bond energy, which is roughly $1\ eV$.

In our comparison, the candidates are one hexagonal shape (H), two square shape $(S_\square$ and $S_\diamond)$ SiNW for two possible surface reconstructions $[(2 \times 1)$ and $c\,(2 \times 2)]$, and two subfamilies of pentagonal shape SiNW $(P_\parallel$ and $P_\perp)$.

Although the energy decomposition is efficient and robust, our TB calculations in Fig. 4.4 underestimate the stacking fault E_f and strain energy (empirical potential calculations are even more). Therefore, instead of using all parameters extracted consistently from only TB results, we use the TB computed E_e's, and *ab initio* computed surface energies and stacking fault $E_f = 0.06\ eV$ [118] and experiment-based shear modulus, $K = 48\ GPa = 5.9\ eV/atom$ [115]. Because the number of surface atoms in pentagonal wires equals the interface atoms in Ref. [118]. Table 4.1 can be used to evaluate the SiNW's energy at arbitrary thickness.

With this decomposition-extrapolation approach, Fig. 4.5 well represents the energies of the wires, for instance, the asymptotic levels at $d \to \infty$ correspond to their

Table 4.1 Parameters (measured per length of a) used to calculate energy of SiNW: $l = 1, 2, 3, ..., N$ is the number of all atoms, s is a number of surface atoms. The surface energy $\gamma_0 = 1.32$ eV for (100)- and (111)-2×1 are based on Ref. [116], while that of $c(2 \times 2)$ relative to 2×1 based on Ref. [113]. The area $\sqrt{3}a^2/2$ per (111) surface atom is used to define s for the H bars.

	N	s	E_e	$\gamma_s - \gamma_0$
$S_\square$	$(8l^2 + 12l + 1)/\sqrt{2}$	$8l/\sqrt{2}$	5.58	0
$S_\diamond$	$(8l^2 + 12l + 1)/\sqrt{2}$	$8l/\sqrt{2}$	3.56	0.077
H	$4l(6l + 1)$	$2l(2 + 2\sqrt{3})$	1.96	0
$P_\parallel$	$10l(2l + 1)$	$10l$	0	0

relative shape-determined surface areas and surface energies. As well as the asymptotic feature, the curves represent more subtle features, including the crossover of the two sub-families of square shape SiNW [113]. Not surprisingly, decomposition-extrapolation approach shows its limitations: the computed edge energy is actually much larger than the simple addition which we use the approach, due to the strain overlap between neighboring edges when the thickness goes down to $d < 1.5$ nm. The direct calculation for $P_\parallel$ of $d = 1.1$ nm is as high as that of one fullerene cluster wire [119] in Fig. 4.5.

According to the classical Wulff's theorem, the hexagonal SiNW is the most competitive candidate for the ground structure, because all the surfaces are either (100) or {111}, and there is no bulk shear or stacking fault energies in a single crystalline structure. However, pentagonal wire still wins out in Fig. 4.5, because pentagonal wire ($P_\parallel$) has one edge less than hexagonal wire (H), which balances the small lost in bulk energy. Surely, when the diameter goes greater than 6 nm, the cost of the
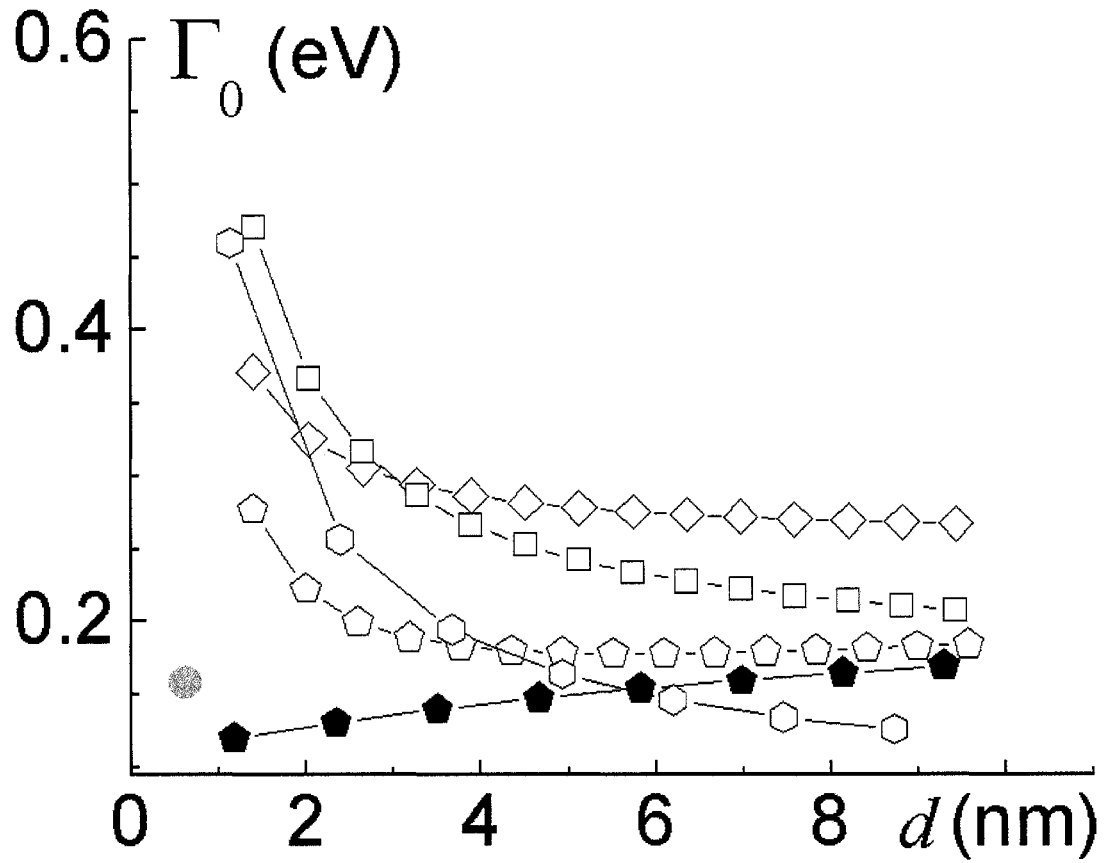
Figure 4.5   Thickness dependent excess surface energy for different families of wires. Open hexagons, squares, and diamonds denote, H, $S_\square$, and $S_\Diamond$ silicon nanowires, respectively. The gray circle is the excess surface energy for the chain of Si_{20} cages, Fig. 5 (c) in Ref. [103].

stacking fault and shear energy eventually overcome the constant benefit from the edge energy. It is consistent with the fact the bulk silicon is the true ground state rather than quasi-crystal or poly-crystal bulk silicon with domain walls inside.

4.2.4   Kinetic Advantages of $P_\parallel$-SiNW and Experimental Evidence

Additional to the energetic stability, the $P_\parallel$ structures also kinetically favor the wire growth due to highly anisotropic diffusion of adatoms on the Si(100)-2×1 surface. It is around 1000 times faster along the flat dimer rows than across the row-groove corrugation [120]. For example, diffusion rate $D = 10^{-9}$ cm^2/s [120], and deposition rate is less than 0.015 ML/s (Mono-layer per second), at a temperature $T = 550$ k. That means adatom propagates to the end of a $1\mu m$ wire faster than two adatom to form a dimer. On $P_\parallel$-SiNW surface, the dimer row is parallel to the axis of the wire. Silicon atoms will prefer to diffuse along the axis, which facilitates the wire to grow in length. On the other hand, $P_\perp$-SiNW surface only allows silicon atoms diffuse in the circumferential direction, which will make the wire goes thicker until it has enough layers to become $P_\parallel$ wire. This kinetics favors a $P_\parallel$-SiNW as well as the energetic stability. In contrast, all other wires do not support such an enhanced axial diffusion.

Besides all these theoretical analysis of both energy and kinetics, several experimental facts indicate that these pentagonal SiNWs are practically synthesizable, or even existing. The silicon multiply-twinned nano-particles (MTP) [121], synthesized
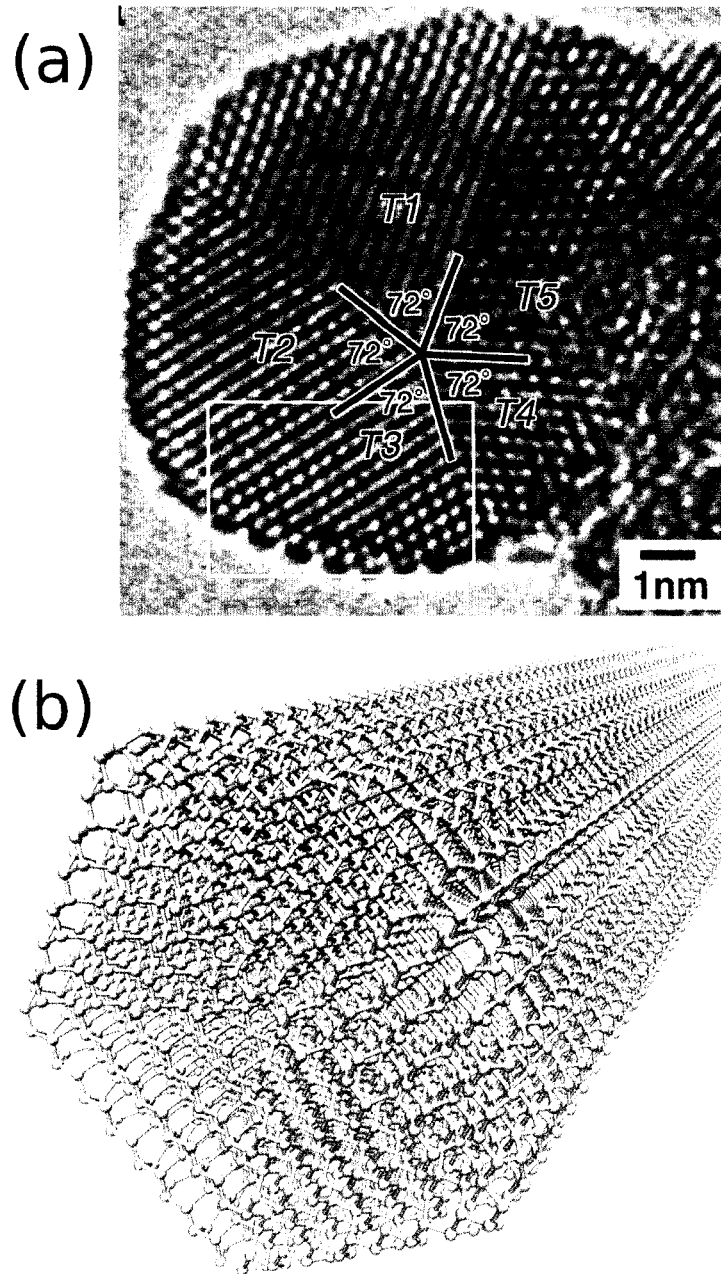
Figure 4.6 Pentagonal silicon nanowire. (a) HRTEM image of a silicon multiply-twinned nano-particle (MTP) with five-folded symmetric cross-section (from Ref. [121]); (b) Ball-and-stick model of a pentagonal silicon nanowire, $P_\parallel$.

by K. Furuya and his colleagues using the electron-induced SiO_2-decomposition technique inside an ultrahigh vacuum transmission electron microscope (UHV-TEM), has five-folded pentagonal-like cross section, shown in Fig. 4.6. The surface reconstruction on the sides of the nano-particle is showing the dimer rows parallel to the direction of the pentagonal-like surface, which is exactly the same as the $P_{\parallel}$-SiNW. Another experimental evidence [103] suggest that high-vacuum growth of SiNW offers an efficient practical way complementary to vapor-liquid-solid growth [100].

4.2.5   Metallic or Semiconducting

As one of the candidates for the next generation of electronic devices, electronic properties of SiNW are the most important but lack of prior research effort. Due to the difficulties in preparation and measurement of individual SiNW with a well defined structure, our theoretical study answers some key questions for the ground structure of $P_{\parallel}$-SiNW, such as what is the electronic band structure, and whether $P_{\parallel}$-SiNW is metal or semiconductor.

Recently, Rurali *et al.* reported on the electronic properties of the square-shaped SiNW [122]. According to their report, surface reconstruction plays a very important role on the conductivity. Different types of surface reconstruction yield completely different behavior: for one kind of reconstruction, SiNW is metallic, while for the other kind of reconstruction, SiNW is semi-metallic. This work indicates that ultra-thin

silicon nanowire may be metallic without any doping.

For the purpose of understanding the physics, we choose the smallest nanowire in the family of $P_{\parallel}$-SiNW, which has a diameter of 1.1 nm, and is shown in Fig. 4.7. The atomistic structure pre-optimized with DFTB method [14] is obtained from previous study. Nevertheless, in order to catch as many details as possible, we employed Density-functional theory (DFT) method to perform all the calculation in this portion of study. We use the hybrid exchange-correlation functional, PBE [26], with the generalized gradient approximation. The basis set we used is a linear combination of numerical atomic orbitals [29], in a double$-\zeta$ polarized form. The plane wave energy cutoff energy is 250 Ry, which is so fine that the energy converges. The Monkhorst-Pack [123] k-point meshes of $[32 \times 1 \times 1]$ are found to provide sufficient accuracy in the calculation of total energies and forces. In order not to exclude the Peierls instability [124], which might change the conductivity from metal to semiconducting, we choose a computational cell with two primitive unit cells along the axis of the nanowire. All the atomic structures are obtained under convergence criteria of the maximum force smaller than 0.04 $eV/\mathring{A}$ and the maximum displacement smaller than 0.01$\mathring{A}$.

After full relaxation, the dimers on the $P_{\parallel}$-SiNW's surface start buckling, which happens to the square-shaped SiNW as well [122], and have been observed in both experiment [125, 126] and calculation [127]. In a buckled dimer, one of the silicon
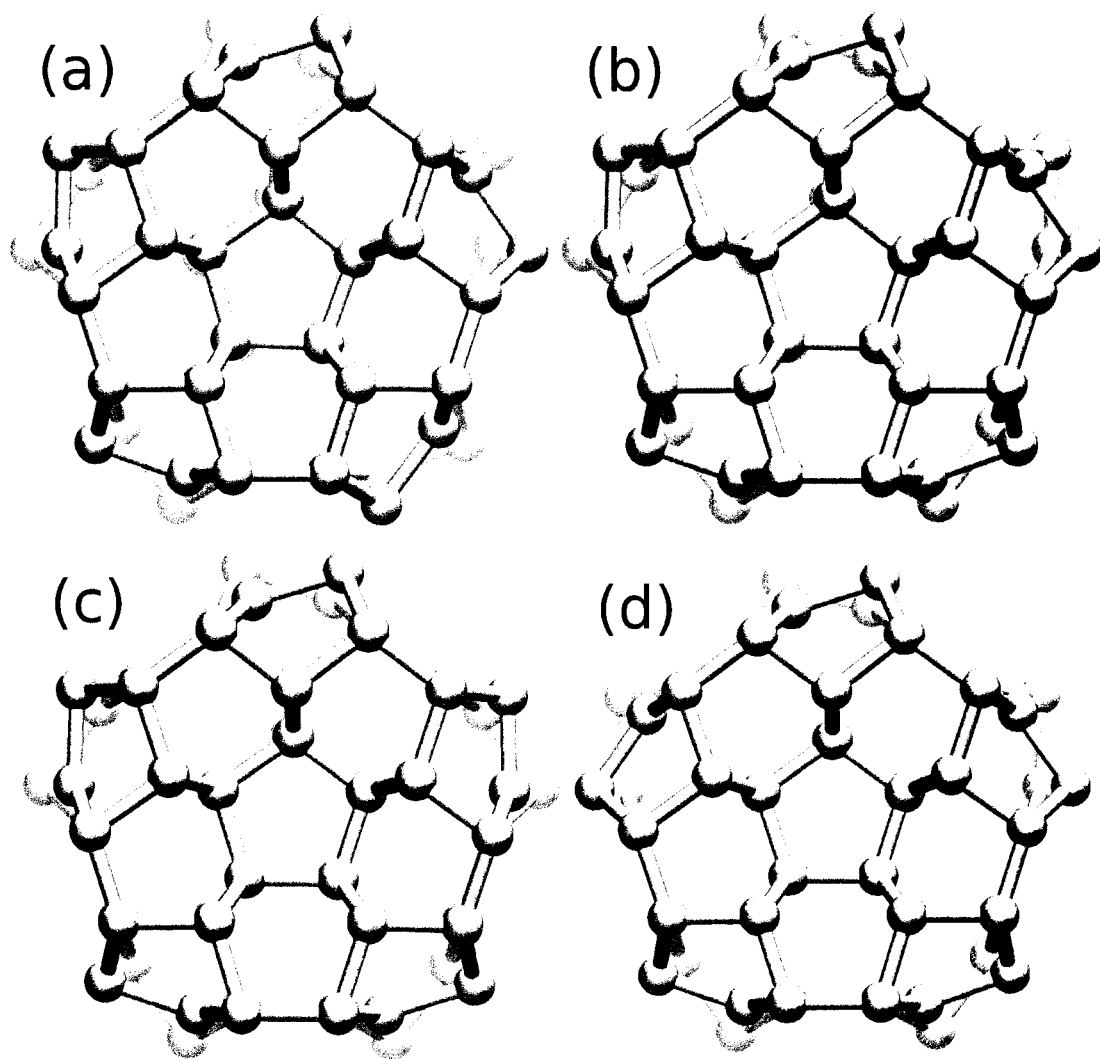
Figure 4.7 Cross sections of the four different buckled pentagonal silicon nanowires.
(a) 5>; (b) 4><; (c) 3>2<; (d) 2><><.

atom pops out of the surface's plane, and the other atom sinks into the plane. This buckled dimer has a degeneracy of two (> and <), because the energy will be the same no matter which atom pops out of the plane. Due to such buckling, the five-folded symmetry is broken. Notably, two adjacent dimers in the same dimer row tend to buckle in different direction, *i.e.* the buckling pattern along the axis is always: ... ><><>< .... However, the neighboring buckles along the circumference do not interact strongly. Consequently, four different buckling patterns are formed, and all are shown in Fig. 4.7: i) 5> (>>>>> or <<<<<); ii) 4>< (>>>>< or <<<<>); iii) 3>2< (>>><< or <<<>>); iv) 2><>< (>><>< or <<><>).

Total energies of these four different buckling patterns are quite close to each other, while the ground state is the first one, 5>. All four energy levels are shown in Fig. 4.9 in reference to the energy of 5>. The highest energy state is 2><><, whose energy is only 0.25 eV higher than 5< per supercell, or 4 $meV/atom$. The lattice constants of these four patterns are also slightly differently from each other. The lattice constant of 5> is the smallest, which is 7.63 $\mathring{A}$, while those for the other three patterns are all 7.67 $\mathring{A}$.

We calculate the electronic band structures for each buckling pattern, and show in Fig. 4.8. Excitingly, all four patterns are conducting, although the DOS of the ground state is semi-metallic. Because there is a small DOS gap open ($\sim$ 50 meV), and the Fermi level is slightly cutting through the conduction band. This gap can be
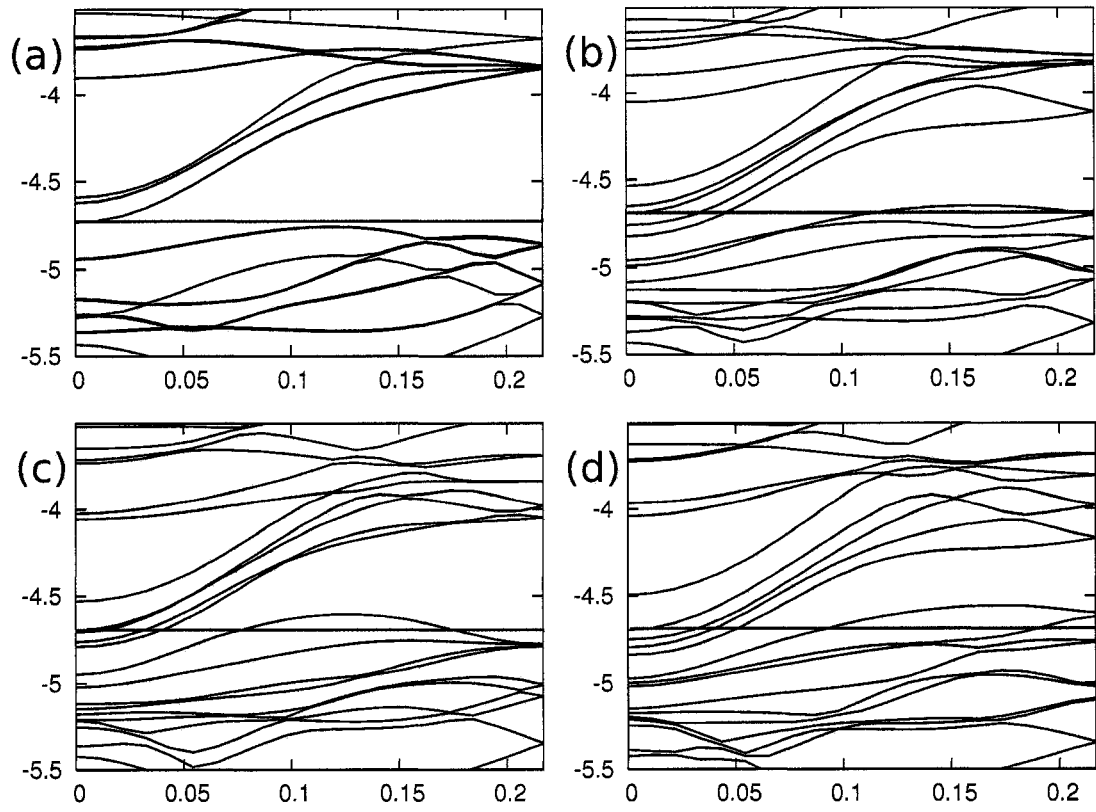
Figure 4.8   Electronic band structures for the four different buckled silicon nanowire $P_{\parallel}$: (a) 5>; (b) 4><; (c) 3>2<; (d) 2><><.

opened wider by applying external strain, which could be proposed for applications of mechanical-electronic sensor.

In Fig. 4.8, one can see that all four band structures have some similarities. For example, the band gap in semi-metallic 5> pattern is indirect: the bottom of the conduction band is located at the Γ point [9], and the top of the valence band is somewhere between Γ point and X point. The band structures for the other three metallic patterns also have the bottom of the conduction band located at the Γ point, and the top of the valence band located between Γ and X points. However, the gaps in the metallic patterns disappear. The top of the valence band drifts away from the Γ point, $i.e.$ the higher the energy pattern, the closer the top of the valence band approaches to the X point.

Since all the energy levels are so close to each other, how stable these patterns are becomes interesting. We calculate the transition barriers between, i) 5> and 4><, ii) 4>< and 3>2<, and iii) 4>< and 2><>< by scanning the potential energy surfaces. Virtually, the transition for each pair of patterns is just a flipping of two buckled dimers. Not surprisingly, the energy barriers are also fairly small, which all less than 270 meV. This indicates that the wire can be easily promoted to metallic states even at room temperature.
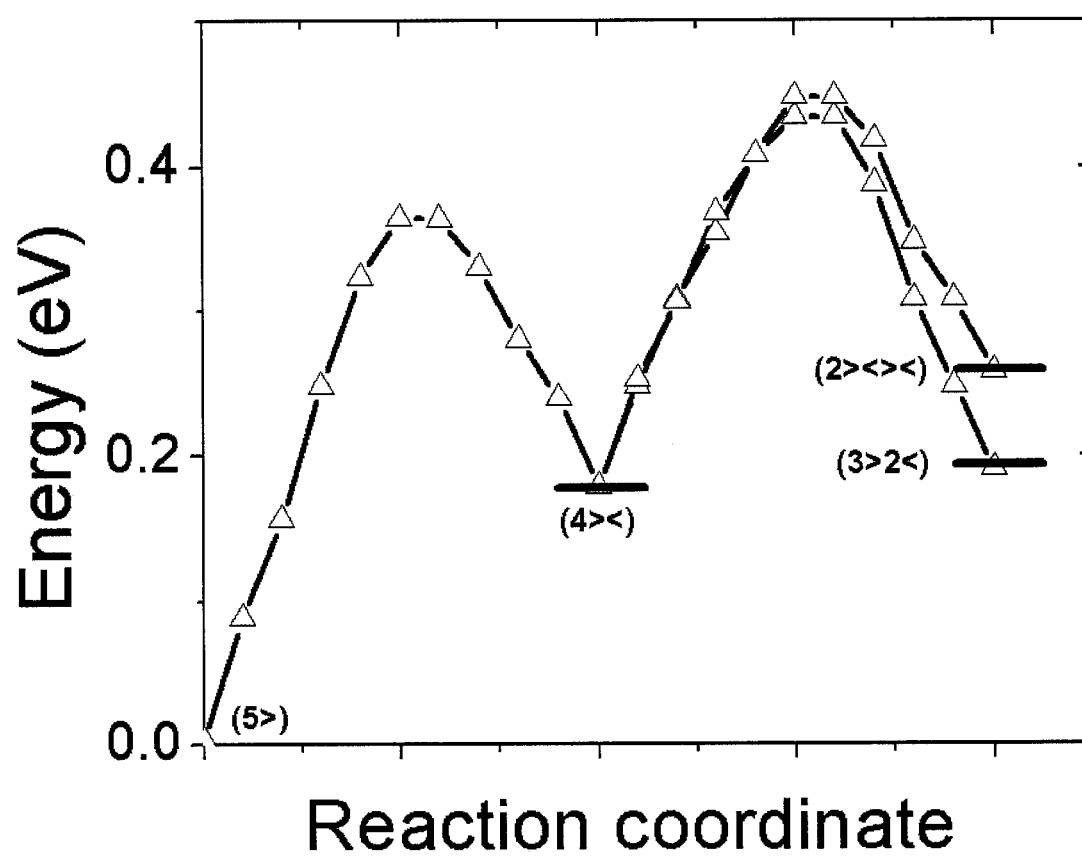
Figure 4.9 Reaction paths between four buckling states of the pentagonal silicon nanowire.

4.3 Hydrogen-Passivated Silicon Nanowires

Pristine SiNW possesses lots of interesting properties, but for most practical applications, pristine SiNW must be passivated prior to any use. Passivated SiNW have been observed in experiments [106] and studied by computational modeling [107, 108, 109, 110]. When surface passivation follows the growth, it effectively seals the wire as it was grown (*e.g.* in high vacuum). Depending on the procedures of synthesis, SiNW can be passivated in many different ways and by variety of agents, *e.g.* hydrogen, oxygen, fluorine, or hydroxyl groups. For simplicity, we only briefly discuss hydrogen passivated nanowires in this section.

In addition to structural stability, we discuss the electronic properties of the pentagonal wires. All the calculations were performed with the Khan's non-orthogonal tight-binding model [15], which is much faster than *ab initio* calculations, yet reasonably accurate in band gap calculations. As a benchmark, we studied a completely hydrogen passivated 3-layer thick hexagonal Si nanowire, which has four {111} and two (100) facets, and is shown in Fig. 4.10. The pseudo-diameter of the single crystalline Si nanowire (before passivation) was defined as $d = \left(32\sqrt{3}/9Nb_{Si}^3/\pi L\right)^{1/2}$, where N is the number of silicon atoms, b_{Si} is the length of Si–Si bond, and L is the periodic length of the Si wire. Thus, the pseudo-diameter of the 3-layer Si wire is 1.3 nm. The tight-binding calculation shows that the band gap of the passivated 3-layer hexagonal Si nanowire is 2.2 eV, which is reasonably close to the experimen-
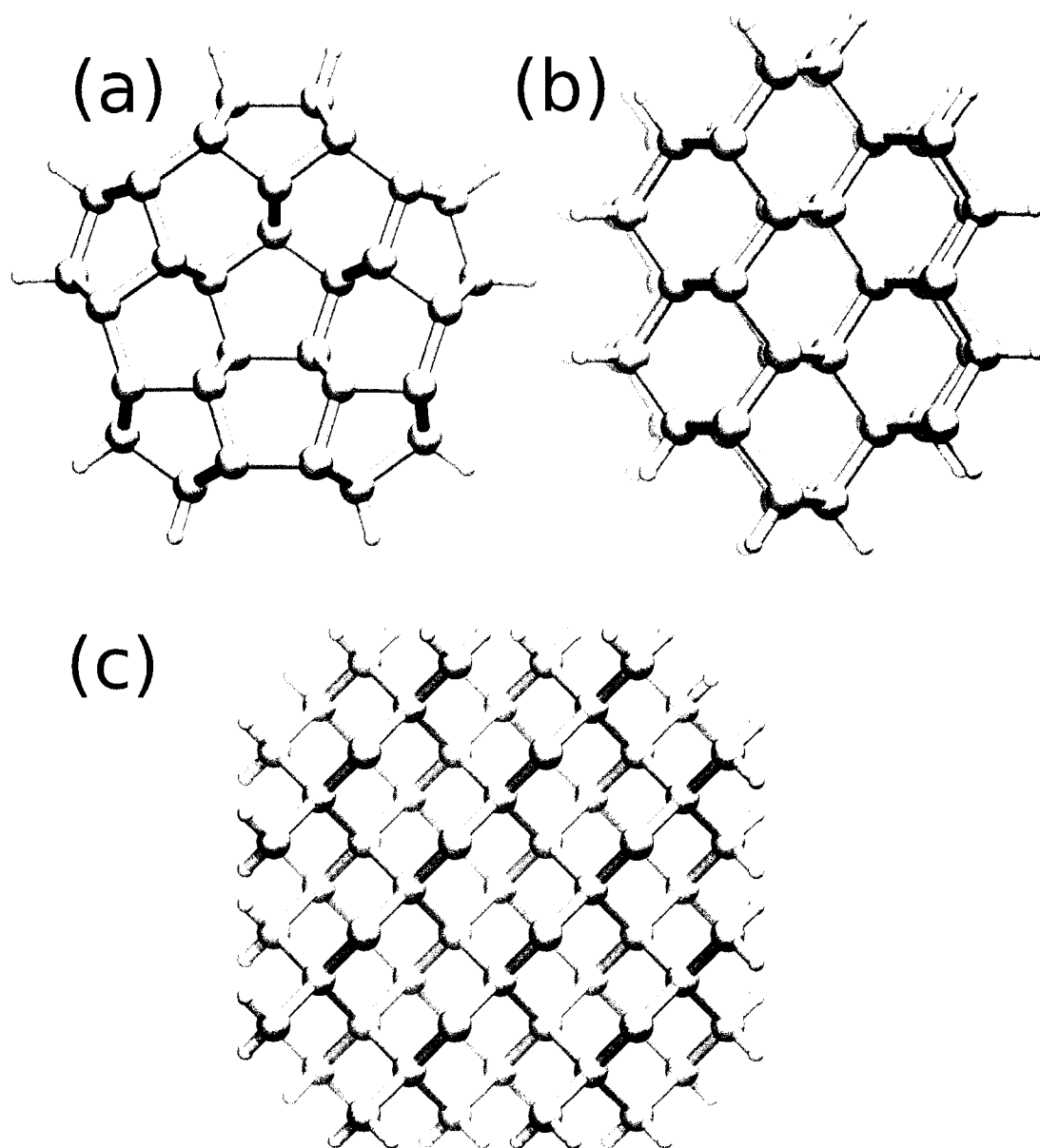
Figure 4.10   Hydrogenated (a) pentagonal silicon nanowire $P_\parallel$, (b) hexagonal <110> silicon nanowire, and (c) square shape cross section (100) silicon nanowire.

tal result [106]. To test the robustness of this tight-binding model for the electronic density of states (DOS) calculations, another single crystalline SiNW with a pseudo-diameter 1.6 nm was studied, which is shown in Fig. 4.10 as well. The cross section of this SiNW is a roughly 8 × 8 square; all the four sides are (100) facets, and four corners are truncated, forming four narrow <110> facets. The band gap for this SiNW is also 2.2 eV, which shows the band gap of passivated SiNW does not depend on the shape of cross section shape much but the pseudo-thickness, and our calculation results are reasonably consistent with the experiments [106].

We first consider $P_{\parallel}$-SiNW, discussed in the previous section as the lowest energy structure. Furthermore, to avoid the rather large systems and to reveal basic physics, the 4-layer pentagonal SiNW $P_{\parallel}$ can be explored. Since there are many ways to passivate this pentagonal SiNW $P_{\parallel}$, we consider fully passivated SiNW, with no dangling bonds left on the surface. Moreover, the pentagonal SiNW $P_{\parallel}$ surface has been dimerized prior to passivation. The structure of this pentagonal SiNW $P_{\parallel}$ is shown in Fig. 4.3. Within the tight-binding approximation, we got the electronic band gap of this passivated 4-layer $P_{\parallel}$-SiNW, $E_g = 2.2\ eV$, which is close to the band gap of the single crystalline SiNW mentioned previously. It also turns out that the shape of the cross section of the SiNW doesn't make much difference for the band gap, but the diameter or thickness play a substantial role to it.

All the results illustrated so far are for the equilibrium structures of different

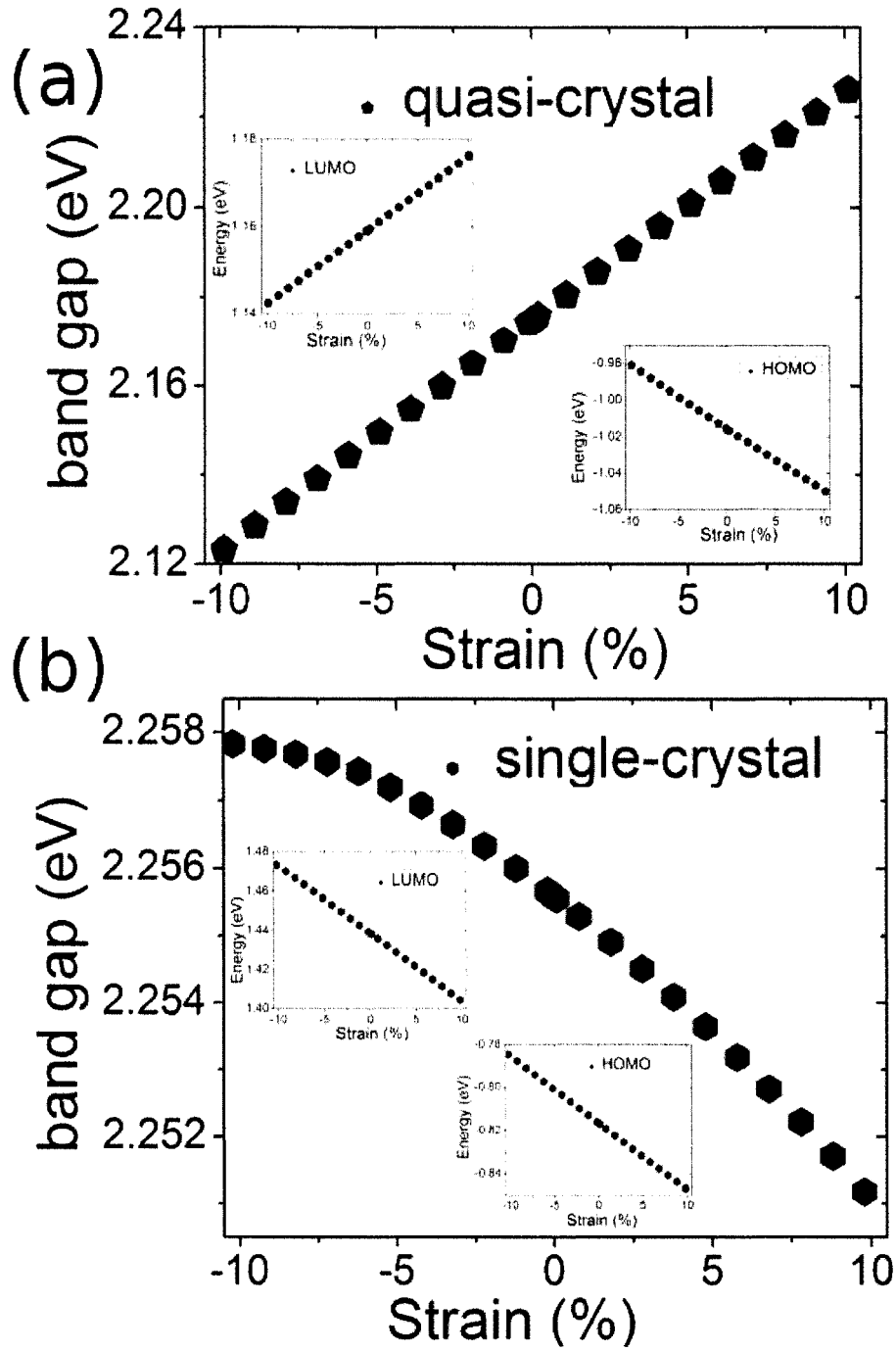
Figure 4.11 Tensile strain dependence of the band gap for the hydrogen-passivated (a) $P_\parallel$ silicon nanowire and (b) hexagonal <110> silicon nanowire; insets are the strain dependence of the HOMO and LUMO energies, respectively.

SiNW's, which have no any external stress or compression. The strain effect on the electronic band structure is well known and has been studied both theoretically [128] and experimentally [129] for decades. For 1D-structures, among recent examples is the band gap change of carbon nanotubes tunable by varying the external strain [130]. We have recently investigated the strain effect on the electronic band gap of SiNW, based on which the strain-controlled switch could be proposed. In Fig. 4.11(a), the band gap of the passivated 4-layer pentagonal $P_\parallel$-SiNW is plotted against the strain applied along the axis of the SiNW. The band gap of this $P_\parallel$-SiNW has a nearly linear response to the uniaxial strain applied on the nanowire,

$$E_g = E_0 + \kappa\epsilon \tag{4.3}$$

where E_0 is the band gap of the equilibrium structure, $\kappa = -0.51\ eV$, and ϵ is the external strain. The band gap of passivated $P_\parallel$ varies by about 120 meV within $\pm 10\%$ strain. For more details, the energies of the highest occupied molecular orbital (HOMO) states and the lowest unoccupied molecular orbital (LUMO) states are plotted respectively in the insets of Fig. 4.11(a). Although both the HOMO and LUMO energies depend linearly on external strain, the corresponding slopes have different sign: LUMO energy increases when the nanowire is stretched, while the HOMO energy linearly decreases.

In contrast, the strain effect to the electronic band gap of the hexagonal single

crystalline SiNW with a similar diameter is different. Here, Fig. 4.11(b), both HOMO and LUMO energies decrease linearly with tension, their slopes have the same signs and are very similar in magnitude. Upon subtraction, the linear term in the band gap is nearly cancelled out, and fitting the gap up to quadratic term yields:

$$E_g = E_0 + \kappa\epsilon + \gamma\epsilon^2 \qquad (4.4)$$

where γ is the second order coefficient of Taylor expansion of $E_g(\epsilon)$. Here, $\kappa = -0.03\ eV$ is twenty times less than for the $P_{\parallel}$ wire, $\gamma = -0.11\ eV$ becomes relatively significant, and makes the band gap dependence nonlinear, although small compared to the $P_{\parallel}$ wire: the band gap varies only by 7 meV between $+10\%$ and -10% strain. Therefore, although both the passivated quasi-crystalline $P_{\parallel}$-SiNW and the passivated single crystalline hexagonal SiNW have band gap tunable by the axial strain, only the band gap in $P_{\parallel}$ changes linearly and significantly, and thus might be of interest for designing an intact nano-sensor of strain, by remotely observing the changing wavelength of light emission.

4.3.1 Mechanical Properties

Mechanical properties of these silicon nanowires are also studied. Following the conventional definition [115, 131], the Young's modulus of passivated silicon nanowire can be estimated from the second derivative of the energy-strain curve:

$$Y = \frac{1}{V_{eff}} \frac{\partial^2}{\partial \epsilon^2} E \bigg|_{\epsilon=0} \qquad (4.5)$$

in which, V_{eff}, is the effective volume for strain-free structure or equilibrium structure, E is the strain energy, and ϵ is the uniaxial strain along the axis of the silicon nanowires. Since in the nano-scale the volume is not well defined, we introduce the effective volume, $V_{eff} = N\nu$, where ν is the volume per atom in silicon bulk, while the volume for hydrogen atoms is neglected. Again, the strain energies are calculated with Khan's orthogonal tight-binding model [15]. The Young's moduli of 4-layered $P_{\parallel}$-SiNW is 145 GPa, which is much stronger than that of the square shape SiNW, 103 Gpa. However, both of them are in the same order of the silicon bulk's modulus, $\sim$ 150 GPa both experiments [132] and computations [115, 131].

4.4 Conclusion

In summary, with assistance of the modified Wulff's theorem, we compared different families of SiNWs and singled out one of the pentagonal shape cross-section SiNW, $P_{\parallel}$ is the ground state of known silicon quasi-1D nano-structure. This $P_{\parallel}$-SiNW has four different surface reconstructions. The ground state of them is semi-metallic, while the other three are all metallic. The transition barrier for conversion between different patterns can be overcome by thermal vibration under room temperature. The band gap of the hydrogen passivated $P_{\parallel}$-SiNW is linear dependent on the external strain, while single crystalline SiNW's are not.

Appendix A

Temperature Dependent Strength

A.1 Low Temperature Limit

In this Appendix, we derive Eq. (3.4).

$$\int_{\bar{x}-a}^{\bar{x}} dx \left(\frac{k_B T}{2\pi\hbar v} \right) e^{-\frac{1}{k_B T}\left(\varepsilon_{ts}-E_0+\frac{1}{2}\gamma_{ts}\frac{a^2}{4} \right)} e^{\frac{1}{k_B T}\left[\frac{1}{2}(\gamma-\gamma_{ts})x^2+\frac{1}{2}\gamma_{ts}ax \right]} = 1 \tag{A.1}$$

$$\int_{\bar{x}-a}^{\bar{x}} dx \cdot e^{\frac{1}{k_B T}\left(\frac{\gamma-\gamma_{ts}}{2} \right)\left(x^2+\frac{\gamma_{ts}}{\gamma-\gamma_{ts}}ax \right)} = \frac{2\pi\hbar v}{k_B T} e^{\frac{1}{k_B T}\left(\varepsilon_{ts}-E_0+\frac{1}{2}\gamma_{ts}\frac{a^2}{4} \right)} \tag{A.2}$$

$$\int_{\bar{x}-a}^{\bar{x}} dx \cdot e^{\frac{1}{k_B T}\left(\frac{\gamma-\gamma_{ts}}{2} \right)\left(x+\frac{\gamma_{ts}}{\gamma-\gamma_{ts}}\frac{a}{2} \right)^2} = \frac{2\pi\hbar v}{k_B T} e^{\frac{1}{k_B T}\left(\varepsilon_{ts}-E_0+\frac{1}{2}\frac{\gamma\gamma_{ts}}{\gamma-\gamma_{ts}}\frac{a^2}{4} \right)} \tag{A.3}$$

$$\sqrt{\frac{\pi k_B T}{2(\gamma-\gamma_{ts})}} erfi\left[\sqrt{\frac{\gamma-\gamma_{ts}}{2k_B T}}x \right]\Bigg|_{\bar{x}+x_0-a}^{\bar{x}+x_0} = \frac{2\pi\hbar v}{k_B T} e^{\frac{1}{k_B T}\left(\varepsilon_{ts}-E_0+\frac{1}{2}\frac{\gamma\gamma_{ts}}{\gamma-\gamma_{ts}}\frac{a^2}{4} \right)} \tag{A.4}$$

$$erfi\left[\sqrt{\frac{\gamma-\gamma_{ts}}{2k_B T}}x \right]\Bigg|_{\bar{x}+x_0-a}^{\bar{x}+x_0} = \sqrt{\frac{8\pi\hbar^2 v^2(\gamma-\gamma_{ts})}{k_B^3 T^3}} e^{\frac{1}{k_B T}\left(\varepsilon_{ts}-E_0+\frac{\gamma\gamma_{ts}}{\gamma-\gamma_{ts}}\frac{a^2}{8} \right)} \tag{A.5}$$

$$\frac{1}{x}e^{\frac{\gamma-\gamma_{ts}}{2k_B T}x^2}\Bigg|_{\bar{x}+x_0-a}^{\bar{x}+x_0} = \frac{2\pi\hbar v(\gamma-\gamma_{ts})}{k_B^2 T^2} e^{\frac{1}{k_B T}\left(\varepsilon_{ts}-E_0+\frac{\gamma\gamma_{ts}}{\gamma-\gamma_{ts}}\frac{a^2}{8} \right)} \tag{A.6}$$

$$\frac{1}{\bar{x}+x_0}e^{\frac{\gamma-\gamma_{ts}}{2k_B T}(\bar{x}+x_0)^2} - \frac{1}{\bar{x}+x_0-a}e^{\frac{\gamma-\gamma_{ts}}{2k_B T}(\bar{x}+x_0-a)^2}$$
$$= \frac{2\pi\hbar v(\gamma-\gamma_{ts})}{k_B^2 T^2} e^{\frac{1}{k_B T}\left(\varepsilon_{ts}-E_0+\frac{\gamma\gamma_{ts}}{\gamma-\gamma_{ts}}\frac{a^2}{8} \right)} \tag{A.7}$$

$$\left(\varepsilon_{ts}-E_0+\frac{\gamma\gamma_{ts}}{\gamma-\gamma_{ts}}\frac{a^2}{8} \right) + k_B T \ln\left[\frac{2\pi\hbar v(\gamma-\gamma_{ts})(\bar{x}+x_0)}{k_B^2 T^2} \right]$$
$$= \frac{1}{2}(\gamma-\gamma_{ts})(\bar{x}+x_0)^2 \tag{A.8}$$

$$\rightarrow \quad f(v) = \gamma \bar{x} \approx \gamma \left[\sqrt{\frac{2\Delta E}{\gamma - \gamma_{ts}} + \frac{2k_B T}{\gamma - \gamma_{ts}} \ln\left(\frac{v}{v_c}\right)} - \frac{\gamma}{\gamma - \gamma_{ts}} \frac{a}{2} \right] \qquad (A.9)$$

A.2   High Temperature Limit

In this appendix, Eq. (3.7) is derived:

$$\Delta E \quad = \quad \gamma a \left(x - \frac{a}{2} \right) \qquad (A.10)$$

$$p(x) \quad = \quad \left(1 + e^{\frac{\Delta E}{k_B T}} \right)^{-1} \qquad (A.11)$$

$$-\frac{dp(x)}{dx} \quad = \quad \left(1 + e^{\frac{\Delta E}{k_B T}} \right)^{-2} \frac{\gamma a}{k_B T} e^{\frac{\Delta E}{k_B T}} \qquad (A.12)$$

$$W \quad = \quad -\int_0^a \Delta E(x + \delta) \frac{dp(x)}{dx} dx \qquad (A.13)$$

$$= \quad k_B T \int_{-\xi_0}^{\xi_0} d\xi \, (\xi + \delta') \frac{e^\xi}{(1 + e^\xi)^2} \qquad (A.14)$$

$$f = \frac{W}{a} \quad \propto \quad \frac{2\pi\hbar\gamma v}{k_B T} e^{\frac{\varepsilon_{ts} - E_0 - \frac{a^2}{8}}{k_B T}} \qquad (A.15)$$

References

1. B. J. Alder and T. E. Wainwright, J. Chem. Phys. **27**, 1208 (1957).

2. J. Tersoff, Phys. Rev. B **38**, 9902 (1988); D. W. Brenner, Phys. Rev. B **42**, 9458 (1990); J. Tersoff, Phys. Rev. B **39**, 5566 (1989).

3. S. Iijima, Nature **56**, 354 (1991).

4. B. I. Yakobson, C. J. Brabec, and J. Bernholc, Phys. Rev. Lett. **76**, 2511 (1996).

5. R. Saito, G. Dresselhaus, and M. S. Dresselhaus, *Physical Properties of Carbon Nanotubes*, (Imperial College Press 1998).

6. N. W. Ashcroft and N. D. Mermin, *Solid State Physics*, (Holt, Rinehart and Winston Press, New York 1976).

7. C. M. Goringe, D. R. Bowler and E. Hernandez, Rep. Prog. Phys. **60**, 1447 (1997).

8. J. C. Slater and G. F. Koster, Phys. Rev. **94**, 1498 (1954).

9. W. A. Harrison, *Electronic Structure and the Properties of Solids*, (Dover, New York 1989).

10. B. T. Sutcliffe, *Fundamentals of Computational Quantum Chemistry*, edited by G. H. F. Diercksen, B. T. Sutcliffe, and A. Veillard, (Reidel Press, Boston 1975).

11. P. R. Wallace, Phys. Rev. **71**, 622 (1947).

12. D. Porezag, T. Frauenheim, T. Koller *et al.* Phys. Rev. B **51**, 12947 (1995).

13. R. Ruralia and E. Hernandez, Comput. Mater. Sci. **28**, 85 (2003).

14. C. Z. Wang, B. C. Pan, and K. M. Ho, J. Phys. Condens. Matter **11**, 2043 (1999).

15. F. S. Khan and J. Q. Broughton, Phys. Rev. B **39**, 3688 (1989).

16. J. Pople and D. Beveridge, *Approximate Molecular Orbital Theory*, (McGraw-Hill, 1970).

17. M. J. S. Dewar *et al.*, J. Am. Chem. Soc. **107**, 3902 (1985).

18. J. J. P. Stewart *et al.*, J. Comput. Chem. **10**, 209 (1989).

19. J. M. Frisch *et al.*, Gaussian 03, Revision C.02, Gaussian Inc., Wallingford CT, 2004.

20. M. J. Field *et al.*, J. Comput. Chem. **21**, 1088 (2000).

21. P. Hohenberg and W. Kohn, Phys. Rev. **136**, B864 (1964); W. Kohn and L. J. Sham, Phys. Rev. **140**, A1133 (1965).

22. D. M. Ceperley and B. J. Alder, Phys. Rev. Lett. **45**, 566 (1980).

23. S. H. Vosko, L. Wilk, and M. Nusair, Can. J. Phys **58**, 1200 (1980).

24. J. P. Perdew, Phys. Rev. B **33**, 8822 (1986).

25. A. D. Becke, J. Chem. Phys. **104**, 1040 (1996).

26. J. P. Perdew, K. Burke, and M. Ernzerhof, Phys. Rev. Lett. **77**, 3865 (1996).

27. C. Lee, W. Yang, R. G. Parr, Phys. Rev. B **37**, 785 (1988).

28. A. D. Becke, J. Chem. Phys. **98**, 5648 (1993).

29. J. M. Soler, E. Artacho, J. D. Gale *et al.*, J. Phys. Condens. Matter **14**, 2745 (2002); http://www.uam.es/siesta

30. W. C. Swope, H. C. Anderson, P. H. Berens *et al.*, J. Chem. Phys. **76**, 637 (1982).

31. D. Frenkel and B. Smit, *Understanding Molecular Simulation: From Algorithms to Application*, 2nd Edition (Academic Press, 2002).

32. K. Huang, *Statistical Mechanics*, (Wiley Press, 1987).

33. S. Nose, Mol. Phys. **52**, 255 (1984); W. G. Hoover, Phys. Rev. A **31**, 1695 (1985).

34. N. Metropolis, A. E. Rosenbluth, M. N. Rosenbluth *et al.*, J. Chem. Phys. **21**, 1087 (1953).

35. P. A. Thrower and R. M. Mayer, Phys. Stat. Sol. A **47**, 11 (1978).

36. G. J. Dienes, J. Appl. Phys. **23**, 1194 (1952).

37. P. R. Wallace, Solid State. Comm. **4**, 521 (1966).

38. J. Abrahamson and R. G. A. R. Maclagan, Carbon **22**, 291 (1984).

39. M. I. Heggie, Carbon **30**, 71 (1992).

40. C. H. Xu, C. L. Fu, and D. F. Pedraza, Phys. Rev. B **48**, 13273 (1993).

41. L. Li, S. Reich and J. Robertson, Phys. Rev. B **72**, 184109 (2005).

42. F. Banhart and P. M. Ajayan, Nature **382**, 433 (1996).

43. F. Banhart, Rep. Prog. Phys. **62**, 1181 (1999).

44. J. Y. Huang *et al.*, Nature **439**, 281 (2006).

45. L. Sun, F. Banhart, A. V. Krasheninnikov *et al.*, Science **312**, 1199 (2006).

46. T. D. Yuzvinsky, W. Mickelson, S. Aloni *et al.*, Nano Lett. **6**, 2718 (2006).

47. F. Ding, K. Jiao, M. Wu *et al.*, Phys. Rev. Lett. **98**, 075503 (2007).

48. F. Ding, K. Jiao, Y. Lin *et al.*, Nano Lett. **7**, 681 (2007).

49. W. Sigle and P. Redlich, Phil. Mag. Lett. **76**, 125 (1997).

50. F. Banhart, P. Redlich and P. M. Ajayan, Chem. Phys. Lett. **292**, 554 (1998).

51. J. Y. Huang, F. Ding, K. Jiao *et al.*, Small **3**, 1735 (2007).

52. J. Y. Huang, S. Chen, Z. F. Ren *et al.*, Phys. Rev. Lett. **98**, 185501 (2007).

53. J. Y. Huang, Nano Lett. **7**, 2335 (2007).

54. F. Hasi, F. Simon and H. Kuzmany, J. Nanosci. Nanotech. **5**, 1785 (2005).

55. D. Orlikowski *et al.*, Phys. Rev. Lett. **83**, 4132 (1999).

56. M. Sternberg *et al.*, Phys. Rev. Lett. **96**, 075506 (2006).

57. S. P. Timoshenko, and J. M. Gere, *Theory of Elastic Stability*, (McGraw-Hill Press 1961).

58. R. L. Murry, D. L. Strout, G. K. Odom *et al.*, Nature **366**, 665 (1993).

59. G. E. Scuseria, Science **271**, 942 (1996).

60. Kroto, H. W. Nature **329**, 529 (1987).

61. D. S. Wilkinson, *Mass Transport in Solids and Fuids*, (Cambridge, 2000).

62. M.-F. Yu, O. Louire, M. J. Dyer *et al.* Science **287**, 637 (2000).

63. S. J. Tans, A. R. M. Verschueren, and C. Dekker, Nature **393**, 49 (1998).

64. T. W. Odom, J.-L. Huang, P. Kim *et al.*, Nature **391**, 62 (1998).

65. M. Bockrath, D. H. Cobden, P. L. McEuen *et al.*, Science **275**, 1922 (1997).

66. P. G. Collins, A. Zettl, H. Bando *et al.*, Science **275**, 1922 (1997).

67. C. Papadopoulos, A. Rakitin, J. Li *et al.*, Phys. Rev. Lett. **85**, 3476 (2000).

68. S. Iijima, Mater. Sci. Eng. **B19**, 172 (1993).

69. M. Ouyang, J.-L. Huang, C. L. Cheung *et al.* , Science **291**, 97 (2001).

70. A. A. Odintsov, Phys. Rev. Lett. **85**, 150 (2000).

71. O. Gulseren, T. Yildrim and S. Ciraci, Phys. Rev. Lett. **87**, 116802 (2000).

72. J. L. Bahr, J. Yang, D. V. Kosynkin *et al.*, J. Am. Chem. Soc. **123**, 6536 (2001).

73. J. P. Lu *et al.*, Phy. Rev. Lett. **79**, 1297 (1997)

74. J.-P. Salvetat *et al.*, Phys. Rev. Lett. **82**, 944 (1999).

75. M.-F. Yu, B. S. Files, S. Arepalli *et al.*, Phys. Rev. Lett. **84**, 5552 (2000).

76. A. Thess *et al.*, Science **273**, 483 (1996); L. A. Girifalco, M. Hodak and R. S. Lee, Phys. Rev. B **62**, 13104 (2000).

77. B. Vigolo *et al.*, Science **290**, 1331 (2000).

78. H. W. Zhu *et al.*, Science **296**, 884 (2002).

79. A. B. Dalton *et al.*, Nature **423**, 703 (2003).

80. S. J. V. Frankland *et al.*, J. Phys. Chem. B **106**, 3046 (2002).

81. J. A. Astrom, A. V. Krasheninnikov, and K. Nordlund, Phys. Rev. Lett. **93**, 215503 (2004).

82. A. Kis *et al.*, Nature Materials **3**, 153 (2004).

83. J. Zhu *et al.*, Nano. Lett. **3**, 1107 (2003).

84. Jonghwan Suhr, Wei Zhang, Pulickel M. Ajayan *et al.*, Nano Lett. **6**, 219 (2006).

85. R. C. Haddon, Science **261**, 1545 (1993).

86. T. Fueno, *The Transition State*, edited by T. Fueno, (Gordon and Breach Press, 1999); S. Glasstone, K. J. Laidler, and H. Hyring, *The Theory of Rate Processes*, (McGraw-Hill Press, New York and London, 1941).

87. T. Dumitrica, and B. I. Yakobson, Phys. Rev. B **72**, 35418 (2005); T. Dumitrica, T. Belytschko, and B. I. Yakobson, J. Chem. Phys. **118**, 9485 (2003); Georgii G. Samsonidze, Guram G. Samsonidze, and B. I. Yakobson, Phys. Rev. Lett. **88**, 65501 (2002).

88. B. N. J. Persson, *Sliding Friction, Physical Properties and Applications*, (Springer Press, Berlin, 2000).

89. A. E. Filippov, J. Klafter, and M. Urbakh, Phys. Rev. Lett. **92**, 135503 (2004).

90. J. R. Rice and A. L. Ruina, J. Appl. Mech. **50**, 343 (1983); T. Baumberger and P. Berthoud, Phys. Rev. B **60**, 3928 (1999); N. Kato, Geophys. J. Int. **147**, 183 (2001); O. Ronsin and K. L. Coeyrehourcq, Proc. R. Soc. Lond. A **457**, 1277 (2001); and the references therein.

91. M.-F. Yu, B.I. Yakobson, and R.S. Rouff, J. Phys. Chem. B **104**, 8764 (2000).

92. A. C. Dillon, K. M. Jones, T. A. Bekkedahl *et al.*, Nature **386**, 377 (1997).

93. F. Ding, Y. Lin, P. O. Krasnov *et al.*, J. Chem. Phys. **127**, 164703 (2007).

94. J. Miyamoto, Y. Hattori, D. Noguchi *et al.*, J. Am. Chem. Soc. **128**, 12636 (2006).

95. V. V. Simonyan, P. Diep, and J. K. Johnson, J. Chem. Phys. **111**, 9778 (1999).

96. Q. Wang and J. K. Johnson, J. Phys. Chem. B **103**, 4809 (1999).

97. S. Patchkovskii, J. S. Tse, S. N. Yurchenko *et al.*, Proc. Natl. Acad. Sci. **102**, 10439 (2005).

98. B. K. Price and J. M. Tour, J. Am. Chem. Soc. **128**, 12899 (2006).

99. D. Appell, Nature **419**, 553 (2002).

100. A. M. Morales and C. M. Lieber, Science **279**, 208 (1998).

101. Y. Huang, X. F. Duan, Y. Cui *et al.*, Science **294**, 1313 (2001).

102. Y. F. Zhang, Y. H. Zhang, N. Wang *et al.*, Appl. Phys. Lett. **72**, 1835 (1998).

103. B. Marsen and K. Sattler, Phys. Rev. B **60**, 11593 (1999).

104. U. Landman, R. N. Barnett, A. G. Scherbakov *et al.*, Phys. Rev. Lett. **85**, 1958 (2000).

105. Y. F. Zhao and B. I. Yakobson, Phys. Rev. Lett. **91**, 35501 (2003).

106. D. D. D. Ma, C. S. Lee, F. C. K. Au *et al.*, Science **299**, 1874 (2003).

107. A. J. Read *et al.*, Phys. Rev. Lett. **69**, 1232 (1992).

108. H. Yorikawa, H. Uchida, and S. Muramatsu, J. Appl. Phys. **79**, 3619 (1996).

109. A. K. Singh, V. Kumar, R. Note *et al.*, Nano Lett. **6**, 920 (2006).

110. X. Zhao, C. M. Wei, L. Yang *et al.*, Phys. Rev. Lett. **92**, 236805 (2004).

111. D. D. D. Ma, C. S. Lee and S. T. Lee, Appl. Phys. Lett. **79**, 2468 (2001).

112. C. Herring, Phys. Rev. **82**, 87 (1951).

113. S. Ismail-Beigi and T. S. Arias, Phys. Rev. B **57**, 11923 (1999).

114. D. Vanderbilt, Phys. Rev. B **36**, 6209 (1987).

115. J. J. Wortman and R. A. Evans, J. Appl. Phys. **36**, 153 (1965).

116. A. A. Stekolnikov, J. Furthmuller, and F. Bechstedt, Phys. Rev. B **65**, 115318 (2002).

117. Y. F. Zhao *et al.*, J. Vac. Sci. Technol. A **18**, 320 (2000).

118. D. Vanderbilt, Phys. Rev. Lett. **59**, 1456 (1987).

119. B.-X. Li, P.-L. Cao, R. Q. Zhang *et al.*, Phys. Rev. B **65**, 125305 (2002).

120. Y. W. Mo, J. Kleiner, M. B. Webb *et al.*, Phys. Rev. Lett. **66**, 1998 (1991).

121. M. Takeguchi, M. Tanaka, H. Yasuda *et al.*, Surf. Sci. **493**, 414 (2001).

122. R. Rurali and N. Lorente, Phys. Rev. Lett. **94**, 26805 (2005).

123. H. J. Monkhorst and J. D. Pack, Phys. Rev. B **13**, 5188 (1976).

124. Charles Kittel, *Introduction to Solid State Physics*, (John Wiley & Sons, 2004).

125. Y. J. Li, H. Nomura, N. Ozaki *et al.*, Phys. Rev. Lett. **96**, 106104 (2006).

126. Y. Sugawara, M. Ohta, H. Ueyama *et al.*, Science **270**, 1646 (1995).

127. K. Cho and J. D. Joannopoulos, Phys. Rev. B **53**, 4553 (1996).

128. H. Zhu, S. Feng, D. Jiang *et al.*, Jpn. J. Appl. Phys. **1**, 6264 (1999).

129. G. E. Pikus and G. L. Bir, Sov. Phys. Solid State **1**, 136 (1959).

130. E. D. Minot, Y. Yaish, V. Sazonova *et al.*, Phys. Rev. Lett. **90**, 156401 (2003).

131. E. Hernandez, C. Goze, P. Bernier *et al.*, Phys. Rev. Lett. **80**, 4502 (1998).

132. B. Bhushan and X. Li, J. Mater. Res. **12**, 54 (1997).